RESEARCH TO DEVELOP AND DEFINE CONCEPTS FOR RELIABLE CONTROL SENSORS - THE SOLID STATE RATE SENSOR

FINAL REPORT

APRIL 1966

CONTRACT NO. NAS 12-25
CONTROL NO. ERC/R&D 65-16

NATIONAL AERONAUTICS AND
SPACE ADMINISTRATION
ELECTRONICS RESEARCH CENTER
575 TECHNOLOGY SQUARE
CAMBRIDGE, MASSACHUSETTS

GPO PRICE $ _____

CFSTI PRICE(S) $ _____

Hard copy (HC) 3.00

Microfiche (MF) .65

ff 653 July 65

Prepared by

GENERAL ELECTRIC COMPANY
LIGHT MILITARY ELECTRONICS DEPARTMENT
AVIONIC CONTROLS BUSINESS SECTION
JOHNSON CITY, NEW YORK

Authors

W. D. GATES
S. B. HAMILTON
J. J. WILCZYNSKI

FOREWORD

This report summarizes the work performed by the General Electric Company, Light Military Electronics Department, Avionic Controls Business Section, Johnson City, New York, to fulfill the requirements of the National Aeronautics and Space Administration contract NAS 12-25, "Research to Develop and Define Concepts for Reliable Control Sensors." This contract was initiated under Control Number ERC/R&D 65-16, and was under the technical cognizance of Mr. Dennis Collins, Control and Information Systems Laboratory, NASA Electronic Research Unit.

The work was performed by the Advance Guidance and Control Unit of the Avionic Controls Business Section, and was directed by Mr. R. C. Wells. Other principal contributors were W. D. Gates, S. B. Hamilton, W. B. Tyler and J. J. Wilczynski.

ABSTRACT

This report describes the results of a development effort in the area of Solid State Rate Sensors.

The solid state rate sensor consists of a free-free beam supported at its nodal points and vibrating in one plane at its fundamental bending frequency. It senses angular rate by detecting the presence of Coriolis forces. Piezoelectric crystals are bonded to the metallic beam and provide the driving force which vibrates the beam at its fundamental frequency. Similar crystals provide the readout of the Coriolis induced vibration.

This report describes the development design, fabrication and test of the Solid State Rate Sensor. On this contract significant advancements have been made in the state-of-the-art, particularly in the areas of crystal-beam bonding, vibration amplitude regulation, and elimination of coupling between the drive and readout axis.

While significant advancements have been made, further development is still required in the areas of temperature stability, damping and "G" sensitivity before the Solid State Rate Sensor is applicable to operational systems.

TABLE OF CONTENTS

LIST OF ILLUSTRATIONS

LIST OF SYMBOLS

Page 4

$\bar{i}, \bar{j}, \bar{k}$ - unit vectors in coordinate system fixed to beam mount

$\bar{I}, \bar{J}, \bar{K}$ - unit vectors in inertial coordinate system

$\bar{r}$ - radius vector of beam particle with respect to mount - ft.

$\bar{\omega}$ - angular velocity of coordinate system fixed to beam with respect to inertial coordinate system - rad/sec

$\omega_x, \omega_y, \omega_z$ - angular velocity in x, y, z coordinates - rad/sec

$\bar{v}$ - velocity of beam particle - ft/sec

$\bar{a}$ - acceleration of beam particle - ft/sec^2

m - mass of beam particle - $\frac{lb.\ sec^2}{ft}$

$\bar{F}$ - force on beam particle - lb.

F_x, F_y, F_z - components of force on beam particle - lb.

Page 5

x, y, z - beam particle coordinates in sensor axes - ft.

$$\dot{x} = \frac{d_x}{d_t} \qquad \ddot{x} = \frac{d^2_x}{d_t^2}, \text{ etc.}$$

f_x, f_y, f_z - transducer forces - lbs.

C_x, C_y, C_z - beam damping - ft. lb. sec.

K_x, K_y, K_z - beam restrain - ft. lbs/rad

ω_c - resonant angular rate of beam in drive plane - rad/sec

Q_c - quality factor - drive

ω_o - resonant angular rate of beam readout plane - rad/sec

Q_o - quality factor - readout

Page 7

ℓ - length of beam - ft.

x_o - maximum beam deflection - ft.

t - time - sec.

ϕ_c - phase angle per equation - rad.

Page 8

f_c, f_o - drive and readout frequencies - cycles/sec.

Page 9

F_c - Coriolis force on beam in readout phase - lbs.

Y(s) - Laplace Transform of y

ω_{zo} - maximum amplitude of ω_z

ω_i - input angular rate - rad/sec

Page 10

ϕ_u, ϕ_ℓ - phase angles per equations - rad.

B_u, B_u - maximum amplitudes per equations - ft.

Page 11

Q_i - quality factor - sensor

Page 12

K - scale factor - ft/rad/sec

Page 14

ω_B - bandwidth - rad/sec

Pages 16, 17 and 18

K_B, K_D, K_E - gain factors - volts/volt

Page 32

E - Young's Modulus - lb/ft^2

G - gravity constant - ft/sec^2

ρ - density - lbs/ft^3

f_1 - fundamental beam frequency - cycles/sec

Page 55

ω_g - angular rate of rate table - rad/sec (unless otherwise specified)

R - radial location of sensor - ft

Section 1

INTRODUCTION

Conventional rate gyros have been developed over the past decade or more to a well designed and sophisticated state. Remaining limitations of these gyros are principally in the areas of life, reliability, threshold, power, and size. The Solid State Rate Sensor has the potential for providing improvements in these areas.

Prior effort had demonstrated feasibility through the building and evaluation of four laboratory models. The work performed during the NASA Phase I program was conducted to investigate known problem areas, to design and build a sensor with improved performance and to evaluate the two units built.

The Solid State Rate Sensor has the following principal advantages:

1) Simplicity and reliability

2) Low production costs

3) Wide dynamic range

4) Good linearity

5) Fast start

6) Low power

Additionally, the Solid State Rate Sensor is easily adapted to meet a wide range of requirements by simple potentiometer adjustment.

GENERAL DESCRIPTION

The Solid State Rate of Turn Sensor is a vibrational device that senses angular rate by the measurement of motions resulting from Coriolis forces. The basic sensor consists of a beam supported at its nodal points in a free-free configuration and driven in one of the major planes at its fundamental bending frequency. In this plane, the particles of the beam have a linear displacement which varies sinusoidally with time. If an input angular rate is applied about the longitudinal axis of the beam, the resulting sinusoidal

Coriolis force causes motion of the beam in the plane normal to the drive plane. This orthogonal sinusoidal motion is proportional to the input rate and the beam driving amplitude.

Piezoelectric crystals are centrally bonded to the metallic beam and a sinusoidal voltage applied to the crystals provides the driving force to vibrate the beam at constant amplitude at its first mode resonant frequency. Crystals located orthogonally to the drive crystals sense the Coriolis induced vibration, and provide the output signal.

An electronic drive circuit maintains a constant beam amplitude at resonant frequency by sensing crystal output from a "feedback" crystal and applying a force to the beam through a "drive" crystal.

The readout circuit amplifies the Coriolis induced beam motion signal and demodulates the signal to provide a dc output proportional to input rates about the longitudinal axis.

PROGRAM GOALS

The following design goals were established at an initial coordination meeting with NASA on July 15, 1965.

Maximum angular rate	50-2000°/s
Frequency response	1000 rad/s
Threshold	.001-.01°/s
Hysteresis	$\leq$.02% full scale
Maximum scale factor	.02V/°/s
Scale factor change	$<$1%
Linearity	$\sim$1% full scale
Null shift	0.1-1°/s
Cross coupling	.01-.1%
"g" sensitivity	$\sim$.001°/s/g^2
Start up time	.2 sec
Temperature range	-20 to 70°C
Power	.5 watt at 28 V dc
Life	1 year

These goals were to provide general guidelines for the subsequent development work.

Section 2

SUMMARY

Development effort on this contract has resulted in improvements in the areas of crystal bonding, sensor mounting, lead dress and electronic design while maintaining the inherent simplicity and reliability of the basic rate gyro. These improvements have, in turn, resulted in significant advancements in the sensor performance. Several of the long range design goals have been achieved. Thresholds are less than .01 degree/second, linearity is better than one percent of full scale and long term drifts of less than .02 degree/second/hour have been achieved.

The development effort on this contract has resulted in obtaining an understanding of the basic sensor parameters and their relationship to sensor performance. Gyro units can now be designed and fabricated with predictable operating characteristics.

Three major improvements in the basic sensor have been realized during this development phase. The bond between crystals and beam have improved both transmissibility and stability. The drive regulator has provided a constant beam amplitude. The separation of drive and readout frequencies has increased frequency response and minimized cross coupling between the two planes.

The degree of progress achieved on this contract is indicated in Table 1 of Section 7. From this table it can be seen that an improvement of more than an order of magnitude has been achieved in the following areas:

1) sensor threshold
2) scale factor change with temperature
3) the short term drift
4) long term drift
5) temperature drift

There are still, however, several problem areas which require further effort. Principal among these are null shift with temperature, "G" sensitivity (an area just uncovered during the test phase of the present contract) and frequency response. The interim phase of this program will consider these areas.

Section 3

ANALYSIS

BASIC THEORY OF OPERATION

The basic element of the Solid-State Gyro is a metal beam of rectangular cross section that is vibrated in its fundamental free-free mode. The amplitude of the vibration is small so that the displacement of the beam particles is approximately linear and varies sinusoidally with time. The operation of the sensor depends upon the measurement of Coriolis forces acting on the beam when it is rotating about its longitudinal axis.

The simplest quantitative description of the theory of operation is obtained by describing the motion of one beam particle in inertial space. If the particle position in a moving coordinate system (these coordinates are fixed in the mount for the beam) $\bar{i}$, $\bar{j}$, $\bar{k}$ is described by the vector

$$\bar{r} = \bar{i}\,x + \bar{j}\,y$$

and the motion of the $\bar{i}$, $\bar{j}$, $\bar{k}$ triad with respect to the inertial triad $\bar{I}$, $\bar{J}$, $\bar{K}$ is described by the angular velocity vector

$$\bar{\omega} = \omega_z\,\bar{k}$$

then the velocity and acceleration of the beam particle are given by

$$\bar{v} = \frac{d\bar{r}}{dt} = \frac{\partial \bar{r}}{\partial t} + \bar{\omega} \times \bar{r}$$

$$\bar{a} = \frac{d\bar{v}}{dt} = \frac{\partial^2 \bar{r}}{\partial t^2} + 2\bar{\omega} \times \frac{\partial \bar{r}}{\partial t} + \frac{\partial \bar{\omega}}{\partial t} \times \bar{r} + \bar{\omega} \times \bar{\omega} \times \bar{r}$$

where $\frac{\partial \bar{r}}{\partial t}$ is the velocity of the particle with respect to the moving co-ordinate system and $\frac{d\bar{r}}{dt}$ is with respect to the inertial system. If the particle mass is m and the general force on the particle is

$$\bar{F} = \bar{i}\,F_x + \bar{j}\,F_y$$

then the particle equation of motion is

$$\frac{1}{m}\bar{F} = \frac{\partial^2 \bar{r}}{\partial t^2} + 2\bar{\omega} \times \frac{\partial \bar{r}}{\partial t} + \frac{\partial \bar{\omega}}{\partial t} \times \bar{r} + \bar{\omega} \times \bar{\omega} \times \bar{r} \qquad (1)$$

Equation (1) written in matrix form is

$$\frac{1}{m}\begin{bmatrix} F_x \\ F_y \end{bmatrix} = \begin{bmatrix} \ddot{x} \\ \ddot{y} \end{bmatrix} + \begin{bmatrix} 0 & -2\omega_z \\ 2\omega_z & 0 \end{bmatrix} \begin{bmatrix} \dot{x} \\ \dot{y} \end{bmatrix} + \begin{bmatrix} -\omega_z^2 & -\dot{\omega}_z \\ \dot{\omega}_z & -\omega_z^2 \end{bmatrix} \begin{bmatrix} x \\ y \end{bmatrix} \qquad (2)$$

The above equation assumes that the beam particles are constrained to move only in the k-y plane and that external forces act only in the x-y directions. These assumptions are valid for the free-free beam vibrating at small amplitudes with the axes defined as in Figure 1. The x-axis is chosen as the "vibrational" axis or the axis of induced vibration. The y-axis is the "output" axis or the direction of the Coriolis force. The z-axis is the input axis. Refer to page vi for nomenclature of special terms.

The general force $\bar{F}$ consists predominately of external transducer forces, such as those produced by surface mounted piezoelectric crystals, and damping and restraint forces of the beam material on the beam particles. Therefore,

$$\begin{bmatrix} F_x \\ F_y \end{bmatrix} = \underset{\text{Transducer}}{\begin{bmatrix} f_x \\ f_y \end{bmatrix}} - \underset{\text{Damping}}{\begin{bmatrix} C_x \dot{x} \\ C_y \dot{y} \end{bmatrix}} - \underset{\text{Restraint}}{\begin{bmatrix} K_x x \\ K_y y \end{bmatrix}} \qquad (3)$$

Equations (2) and (3) can be combined to give

$$\frac{1}{m}\begin{bmatrix} f_x \\ f_y \end{bmatrix} = \begin{bmatrix} \ddot{x} \\ \ddot{y} \end{bmatrix} + \begin{bmatrix} \frac{\omega_c}{Q_c} & -2\omega_z \\ 2\omega_z & \frac{\omega_o}{Q_o} \end{bmatrix} \begin{bmatrix} \dot{x} \\ \dot{y} \end{bmatrix} + \begin{bmatrix} \omega_c^2 - \omega_z^2 & -\dot{\omega}_z \\ \dot{\omega}_z & \omega_o^2 - \omega_z^2 \end{bmatrix} \begin{bmatrix} x \\ y \end{bmatrix} \qquad (4)$$

Equation (4) is the description of beam particle motion with transducer forces and input angular rates. It can be generalized to the entire beam by noting that the deflection of the beam as a function of position along the beam and time is given approximately by

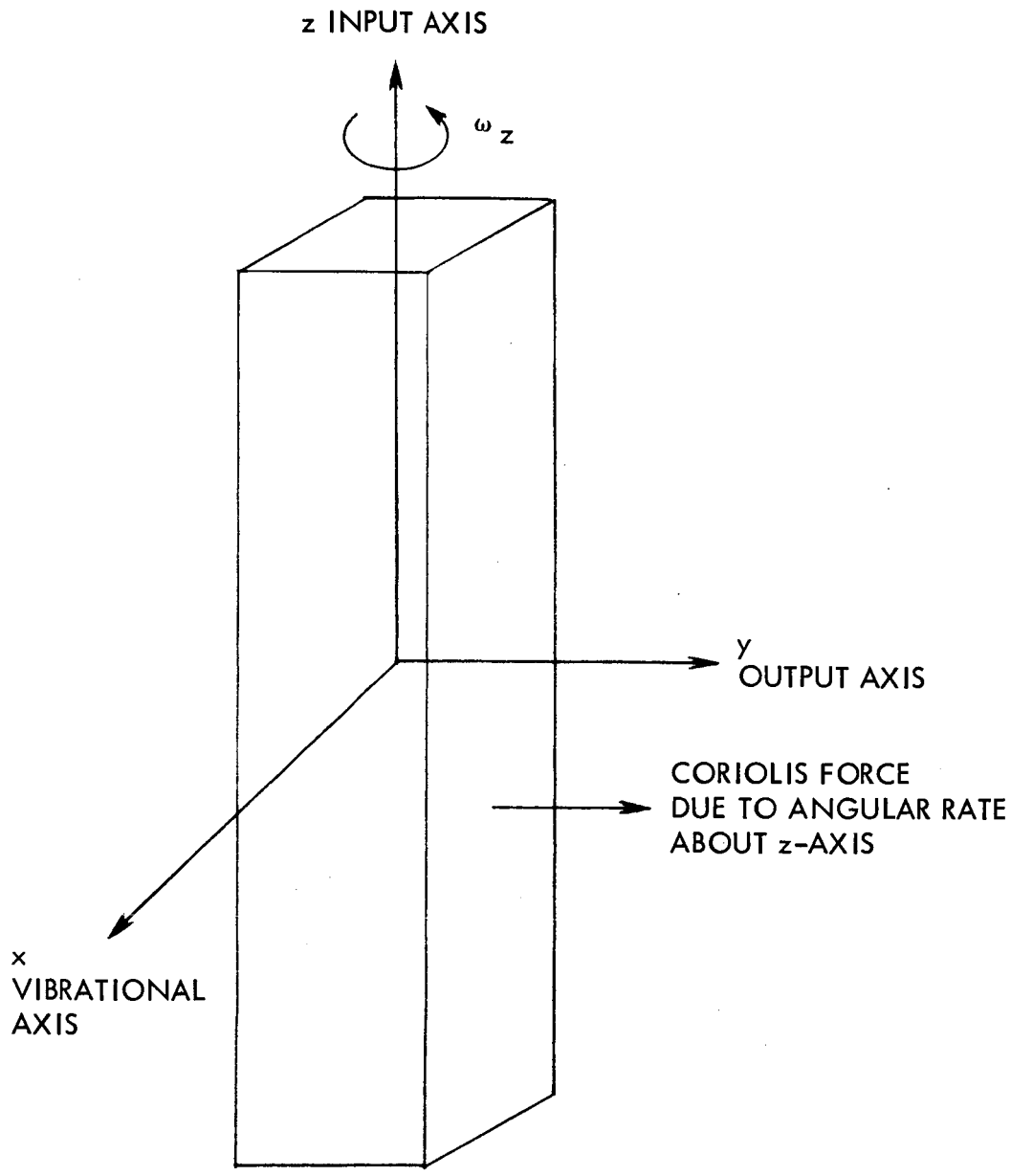

Figure 1. Solid State Rate Sensor Axes

$$x(z,t) = \left[x_o \sin \frac{\pi z}{\ell} - a\right] \cos \omega_c t \quad \text{(see Appendix B)}$$

where ℓ is the length of the beam and ω_c is the resonant frequency in the vibrational axis. Therefore, the motion of individual particles varies only in amplitude along the beam.

The sensitivity of the Solid State Gyro to a constant rate ω_z is found from equation (4) by assuming that f_x is controlled such that the deflection x(t) is

$$x(t) = x_o \sin \omega_c t,$$

$f_y = o$ and $\omega_c >> \omega_z$. The deflection of the beam in the output axis under these conditions is given by the solution to the following equation

$$-2\omega_z \omega_c x_o \cos \omega_c t = \ddot{y}(t) + \frac{\omega_o}{Q_o} \dot{y}(t) + \omega_o^2 y(t)$$

The steady-state solution to the above equation is

$$y(t) = \frac{2x_o \omega_z}{\omega_c \left[\left(1 - \frac{\omega_c^2}{\omega_o^2}\right)^2 + \left(\frac{\omega_c}{\omega_o Q_o}\right)^2\right]^{1/2}} \cos\left(\omega_c t - \phi_c\right) \qquad (5)$$

where $\phi_c = \arctan\left[\frac{\omega_c \omega_o}{Q_o\left(\omega_o^2 - \omega_c^2\right)}\right]$

Therefore, the output deflection is proportional to both the amplitude of vibration in the x-axis and the input angular rate, and is a function of the relative locations of the resonant frequencies in the vibration and output axes.

RESONANT FREQUENCY SEPARATION

One of the significant design parameters of the Solid State Angular Rate Sensor is the separation of the resonant frequencies in the drive and readout planes. The separation affects the gain, null stability and bandwidth of the sensor. If the two frequencies are equal, the gain of the rate

sensor is high due to the Q of the output plane, and the null of the device is unstable because of the electrical and mechanical coupling between drive and readout planes. If the frequencies are separated widely, the gain is low and the null is stable due to the absence of coupling. Also, the bandwidth of the Solid State Angular Rate Sensor is approximately equal to the frequency separation and thus, influences the specification of the separation.

Experimental and theoretical results show that the beam of the Solid State Angular Rate Sensor should be designed so that the resonant frequencies in the two planes are separated to eliminate phase coupling. That is, the phase shift due to the output plane dynamics is below a specified minimum (i.e., 1 degree). The separation of frequencies has three distinct advantages:

1) Minimizes the effects of output plane dynamics on the performance of the rate sensor.
2) Provides proper phasing of transducer voltages and facilitates processing of the sensor output.
3) Provides sufficient bandwidth for the rate sensor.

In the following analysis, the effects of frequency separation are shown quantitatively, the optimum separation is derived, and the functional relationship between separation and sensor bandwidth is delineated.

In order to maintain accurate phasing of electrical signals and eliminate coupling between the two planes, the phase angle ϕ_c must be kept small. If the maximum allowable value of ϕ_c is ϕ_o and $\tan \phi_o \simeq \phi_o$, then

$$\phi_o \simeq \frac{\omega_c \omega_o}{Q(\omega_o^2 - \omega_c^2)}$$

The above equation can be solved for the required relationship between f_c and f_o.

$$f_o - f_c \simeq \frac{f_o}{2\phi_o Q_o} \qquad (6)$$

Equation (6) gives the frequency separation in terms of the maximum allowable phase shift, ϕ_o, and the Q_o of the output plane. For instance, if the resonant frequency in the output plane is 1500 cps, $Q = 500$, and $\phi_o = 1.0^o$ then the beam must be designed for a frequency separation of 85 cps.

FREQUENCY RESPONSE

The following analysis determines the frequency response of the Solid State Angular Rate Sensor to a sinusoidal input rate. The response of the beam in the readout or output direction is given by the solution to

$$\ddot{y}(t) + \frac{\omega_o}{Q_o}\dot{y}(t) + \omega_o^2 y(t) = \frac{f_c(t)}{m}$$

In Laplace transform notation,

$$Y(s) = G(s)\frac{F_c(s)}{m\omega_o^2}$$

where

$$G(j\omega) \simeq \frac{1}{2\left(1 - \frac{\omega}{\omega_o}\right) + \frac{j}{Q_o}}$$

for large Q_o and operating frequencies near the resonant frequency ω_o.

Therefore,

$$\left|G(j\omega)\right| \simeq \frac{1}{\left[4\left(1 - \frac{\omega}{\omega_o}\right)^2 + \frac{1}{Q_o^2}\right]^{1/2}} \triangleq B(\omega)$$

$$\text{Arg } G(j\omega) = -\tan^{-1}\left[\frac{1}{2Q_o\left(1 - \frac{\omega}{\omega_o}\right)}\right] = \phi(\omega)$$

If the oscillating input angular rate for the sensor is given by

$$\omega_z(t) = \omega_{zo}\cos\omega_i t$$

then the Coriolis force on the beam, $f_c(t)$, is given by

$$f_c(t) = -2mx_o\omega_{zo}\omega_c\cos\omega_i t\cos\omega_c t$$

where the motion of the beam in the drive plane is

$$x(t) = x_o \sin \omega_c t$$

and ω_c is the resonant frequency of the drive plane.

Then,

$$f_c(t) = -m\, x_o\, \omega_{zo} \omega_c \left[\cos (\omega_c + \omega_i)t + \cos (\omega_c - \omega_i)t\right]$$

The Coriolis force for an oscillating input rate has then two frequency components or sidebands, $\omega_c + \omega_i$ and $\omega_c - \omega_i$. The attenuation and phase shift of these sidebands by the dynamics of the beam in the output plane determines the bandwidth of the rate sensor. If the beam is designed for a resonant frequency separation between the drive and readout planes such that there is minimual phase coupling, then the response of the sensor depends almost entirely on the upper sideband response. As the input frequency ω_i increases, the lower sideband is attenuated and remains at approximately zero degrees phase shift. However, the upper sideband is amplified and phase shifted by the dynamics of the output plane as $\omega_c + \omega_i$ approaches ω_o. Because of the high Q and narrow bandwidth of the output plane, the predominate response is due to the upper sideband. For the Coriolis force above, the steady-state motion of the beam in the readout plane can be found to be

$$y(t) = B_u \cos \left[(\omega_c + \omega_i)t + \phi_u\right] + B_\ell \cos \left[(\omega_c - \omega_i)t + \phi_\ell\right]$$

where

$$B_u = \frac{-x_o \omega_{zo} \omega_c}{\omega_o^2} B (\omega_c + \omega_i), \quad \phi_u = \phi (\omega_c + \omega_i)$$

$$B_\ell = \frac{-x_o \omega_{zo} \omega_c}{\omega_o^2} B (\omega_c - \omega_i), \quad \phi_\ell = \phi (\omega_c - \omega_i)$$

In order to decouple the dynamics of the drive and readout planes of the beam, the resonant frequencies of the planes are separated such that $\omega_c > \omega_o$ and $\phi(\omega_c) \simeq 0$. Refer to equation (6). Therefore, the phase shift of the lower

sideband, $(\omega_c - \omega_i)$, is always approximately zero.

$$\phi_\ell \simeq 0 \text{ for all } \omega_i$$

Using this fact and expanding the expression for y(t), we obtain

$$y(t) = B_u \cos \phi_u \cos \omega_c t \cos \omega_i t - B_u \cos \phi_u \sin \omega_c t \sin \omega_i t$$

$$- B_u \sin \phi_u \sin \omega_c t \sin \omega_i t - B_u \sin \phi_u \cos \omega_c t \sin \omega_i t$$

$$+ B_\ell \cos \omega_c t \cos \omega_i t + B_\ell \sin \omega_c t \sin \omega_i t$$

The only components of the output motion y(t) that produce an electrical rate output for the Solid State Angular Rate Sensor are those which are in phase with the driving force in the input plane (terms containing $\cos \omega_c t$) because of the phase-sensitive demodulation of the output signal. If $y_o(t)$ is the demodulated output of the sensor, then

$$y_o(t) = A(\omega_i) \cos [(\omega_i t - \theta(\omega_i)]$$

where

$$A(\omega_i) = [(B_u \cos \phi_u + B_\ell)^2 + (B_u \sin \phi_u)^2]^{1/2}$$

$$\theta(\omega_i) = \arctan \left[- \frac{B_u \sin \phi_u}{B_u \cos \phi_u + B_\ell} \right]$$

By substituting the expressions for B_u, B_ℓ, etc., and manipulating, we obtain:

$$A(\omega_i) \simeq \frac{x_o \omega_{zo} \omega_c}{\omega_o (\omega_o - \omega_c) \left[4 \left(1 - \frac{\omega_i}{\omega_o - \omega_c} \right)^2 + \frac{1}{Q_i 2} \right]^{1/2}}$$

Multiplied by:

$$\left[1 + \frac{1 - \frac{\omega_i}{\omega_o - \omega_c}}{1 + \frac{\omega_i}{\omega_o - \omega_c}} + \frac{4\left(1 - \frac{\omega_i}{\omega_o - \omega_c}\right)^2 \frac{1}{Q_i^2}}{4\left(1 + \frac{\omega_i}{\omega_o - \omega_c}\right)^2} \right]^{1/2}$$

$$\theta(\omega_i) \simeq \arctan \left[\frac{1}{2Q_i \left(1 - \frac{\omega_i}{\omega_o - \omega_c}\right)} \right]$$

where $$Q_i = \frac{Q_o (\omega_o - \omega_c)}{\omega_o} \qquad (7)$$

The gain and phase of the above expressions are approximately those of a second-order system with a resonant frequency of $\omega_o - \omega_c$ and a quality factor of Q_i. Therefore, the frequency response of the Solid State Angular Rate Sensor is approximately

$$Y(s) = \frac{K}{1 + \frac{s}{Q_i (\omega_o - \omega_c)} + \frac{s^2}{(\omega_o - \omega_c)^2}} \omega_z(s) \qquad (8)$$

where K = scale factor

The above theoretical results have been verified experimentally with frequency response data for an operating Solid State Angular Rate Sensor. Figure 2 gives the frequency response of a sensor that was taken using an oscillating rate table. The drive and readout plane resonances of this particular beam-transducer combination were 1594.7 cps and 1642.2 cps respectively. The Q of the readout plane was 864. Therefore, $f_o - f_c = 47.5$ cps and $Q_i = 25.0$. The data that is plotted in Figure 2 exhibits a resonance at 47 cps with a Q of 22.9, which agrees with the theoretical predictions.

The frequency response exhibited by the SSARS* through both analysis and test indicates that the device has a very lightly damped response and as such is subject to noise at the critical frequency $f_o - f_c$. The chief sources of noise for the sensor are angular accelerations of the beam about its sensitive axis and linear accelerations of the beam mount. Both of the above

*Solid State Angular Rate Sensor

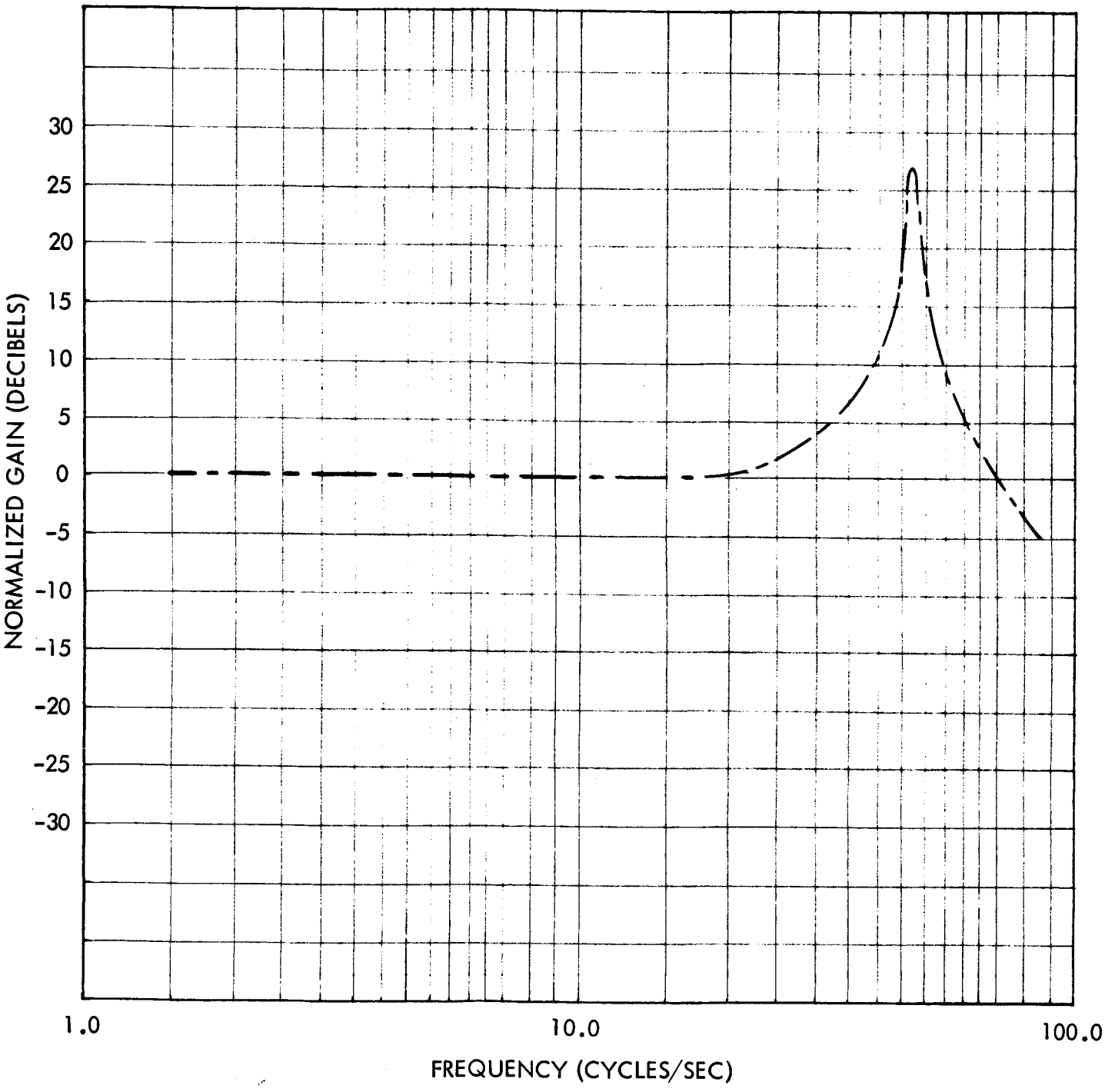

Figure 2. Frequency Response (Unit No. 1)

can produce large amplitude oscillations of the electrical output of the Solid State Sensor. This problem is the most probable cause of short term drift.

AMPLITUDE REGULATION

The drive circuit of the original SSARS had an open loop type of amplitude control. A constant drive voltage was applied to the drive crystal. Changes in beam Q or transducer or bond characteristics resulted in a change in beam amplitude. Tests run on the output voltage of the spare crystal in the drive plane showed that the scale factor of the sensor remains essentially constant for a constant feedback voltage from the crystal. This is shown in Figure 3.

There are two basic approaches which can be used to achieve amplitude regulation; the dc reference method, and the ac reference method. Both compare the feedback voltage to a reference voltage and generate an error signal to drive the beam. These methods are shown in block diagram form in Figures 4 and 5 . During work on the contract, both types of regulators were built. The dc regulator proved most satisfactory and was used in the two units built.

In the dc regulator, Figure 4 , the feedback voltage is demodulated to obtain a dc voltage which is then subtracted from the dc reference voltage. The error signal is modulated at the loop frequency, amplified and added to the loop signal to either increase or decrease the drive voltage.

Tests conducted with the dc regulator circuits and the beam-transducer combination indicated that one percent regulation of feedback could be obtained. The regulation depends only on the choice of gain for the error amplifier and stability considerations (compensation is needed for higher gains). It was found that the third harmonic content of the drive voltage was acceptable with this approach.

The accuracy and stability of the feedback voltage regulation are dependent upon the gains and frequency responses chosen for the various elements in the loop. Consider the block diagram shown in Figure 6. The dynamics of the beam and transducers are the response to an amplitude modulated drive voltage whose carrier is the resonant frequency of the drive plane ω_c. The bandwidth ω_B is given approximately by

$$\omega_B \simeq \frac{\omega_c}{2Q} \quad \text{for high Q}$$

The transfer function of the peak detector and compensation H(s) is chosen for noise rejection and stability. Typically,

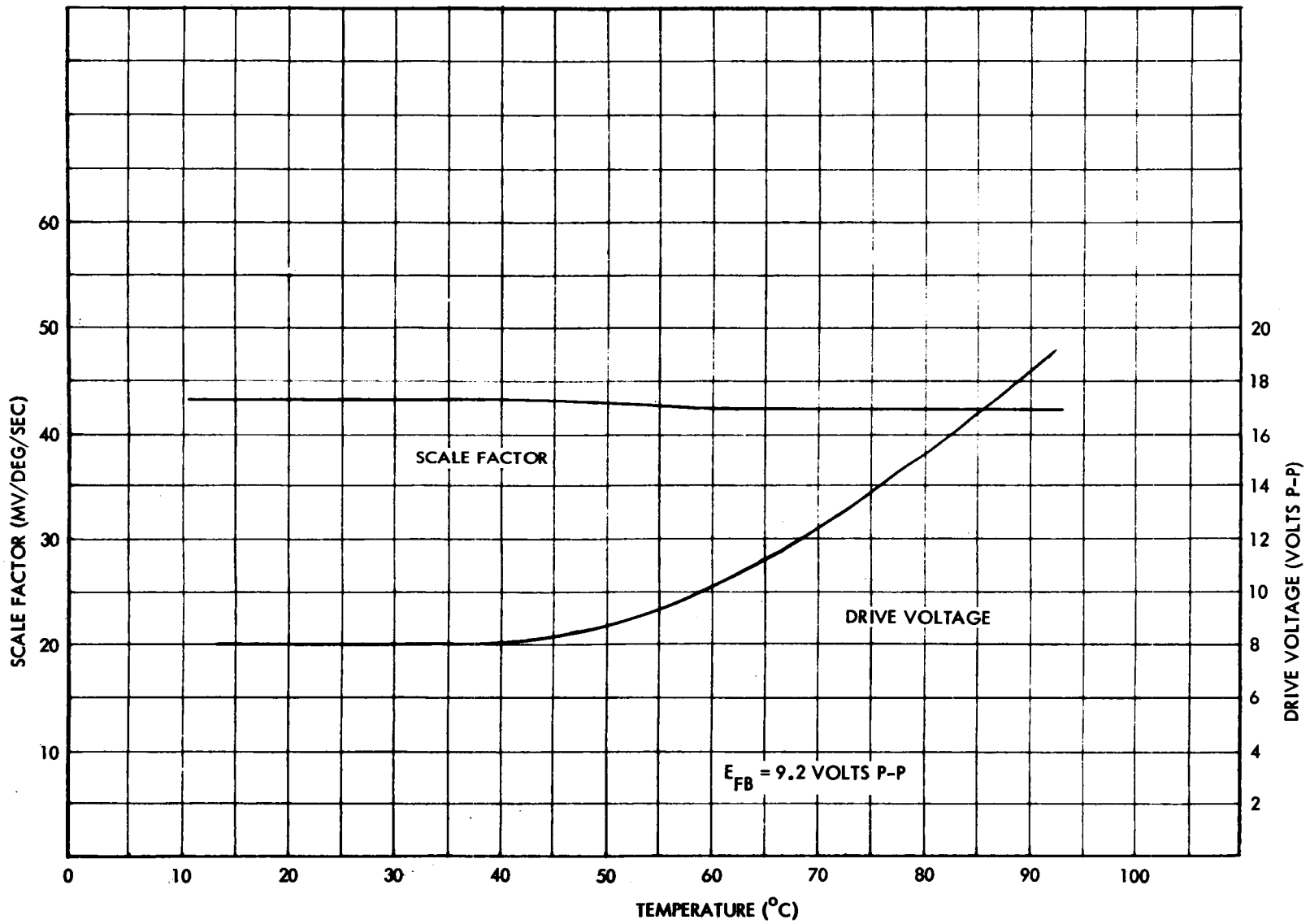

Figure 3. Scale Factor and Drive Voltage Vs. Temperature For Constant Feedback Voltage

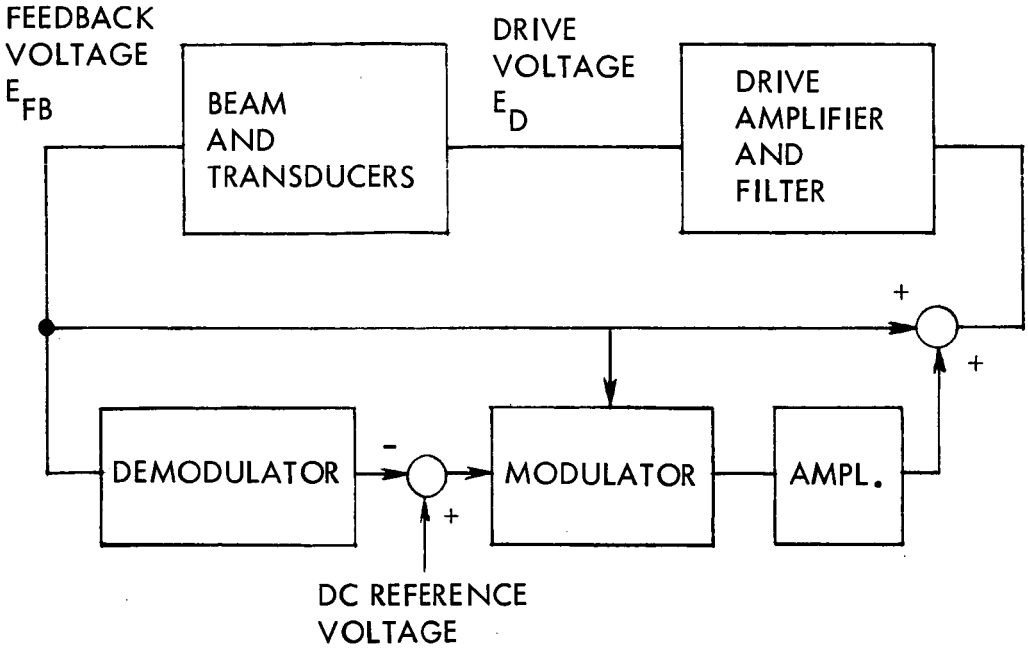

Figure 4. Amplitude Control Using DC Reference

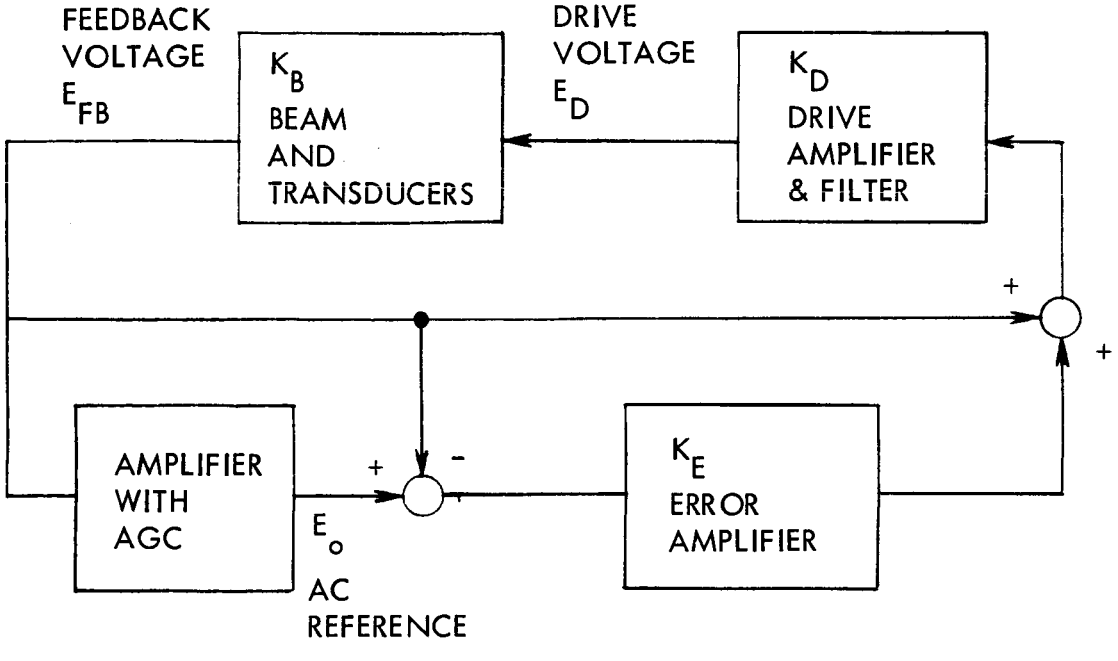

Figure 5. Amplitude Control Using AC Reference

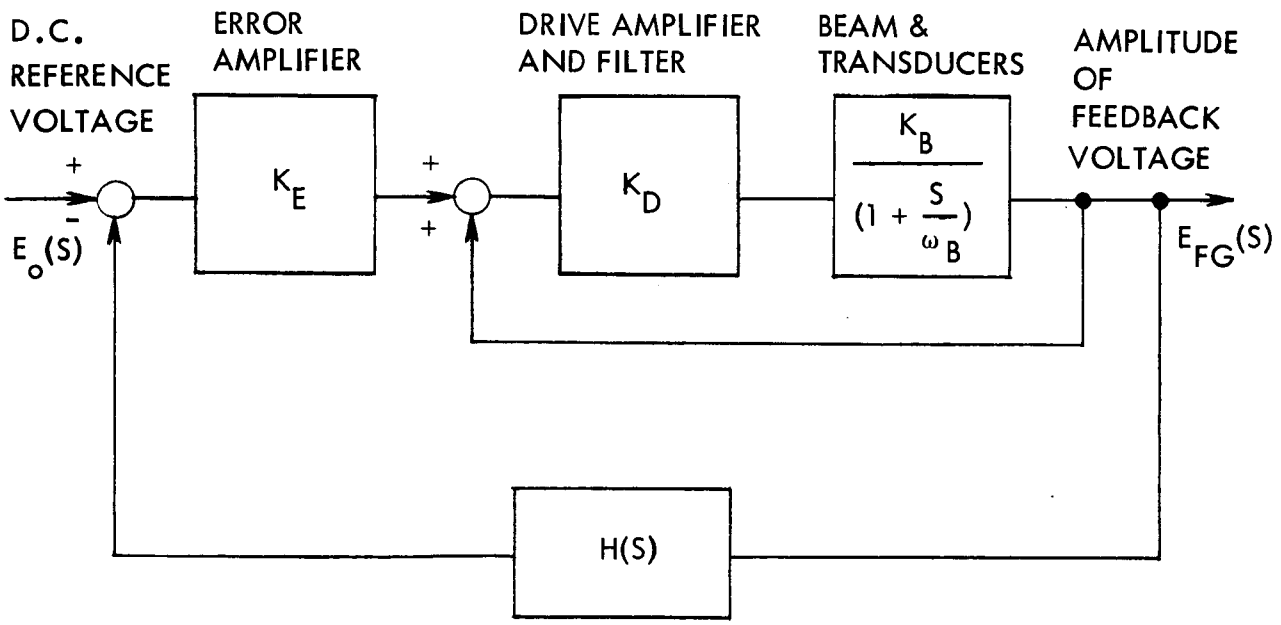

$$\text{TYPICAL } H(S) = \frac{(1 + \frac{S}{\omega_2})}{(1 + \frac{S}{\omega_1})(1 + \frac{S}{\omega_2})} \quad , \omega_1 < \omega_2 < \omega_3$$

Figure 6. Amplitude Regulation Block Diagram

$$H(s) = \frac{(1 + \frac{s}{\omega_2})}{(1 + \frac{s}{\omega_1})(1 + \frac{s}{\omega_3})} \quad \text{with } \omega_1 < \omega_2 < \omega_3$$

The outer loop gain for the block diagram is

$$A(s) = \frac{K_D K_B K_E \ (1 + \frac{s}{\omega_2})}{(1 - K_D K_B)(1 - \frac{s}{\omega'_B})(1 + \frac{s}{\omega_1})(1 + \frac{s}{\omega_3})}$$

where $\omega'_B = \omega_B (K_D K_B - 1)$.

The drive amplifier gain is usually chosen such that $K_D K_B > 1$ for all possible values of K_B so that A(s) always has a right-half plane pole.

The closed loop response of the system is given by

$$\frac{E_{FB}(s)}{E_o(s)} = \frac{K_D K_B K_E \ (1 + \frac{s}{\omega_1})(1 + \frac{s}{\omega_3})}{(1 - K_D K_B)(1 - \frac{s}{\omega_{B'}})(1 + \frac{s}{\omega_3})(1 + \frac{s}{\omega_1}) + K_D K_B K_E \ (1 + \frac{s}{\omega_2})}$$

and to find regulation accuracy

$$E_{FB} = \frac{K_D K_B K_E}{1 + K_D K_B (K_E - 1)} \ E_o$$

Note that for $K_D K_B > 1$ and large K_E, that the feedback voltage is always larger than the reference. In $K_D K_B = 2$, $K_E = 50$ produces two percent regulation of E_{FB} and $K_E = 100$ produces one percent regulation.

By using a nominal K_E of 50 and $K_D K_B = 2$, the location of the critical frequencies of H(s) can be determined for stability considerations.

A typical Bode plot of the open loop gain $A(j\omega)$ is shown in Figure 7. The frequency f_B of the beam and transducer combination of this case is one cps.

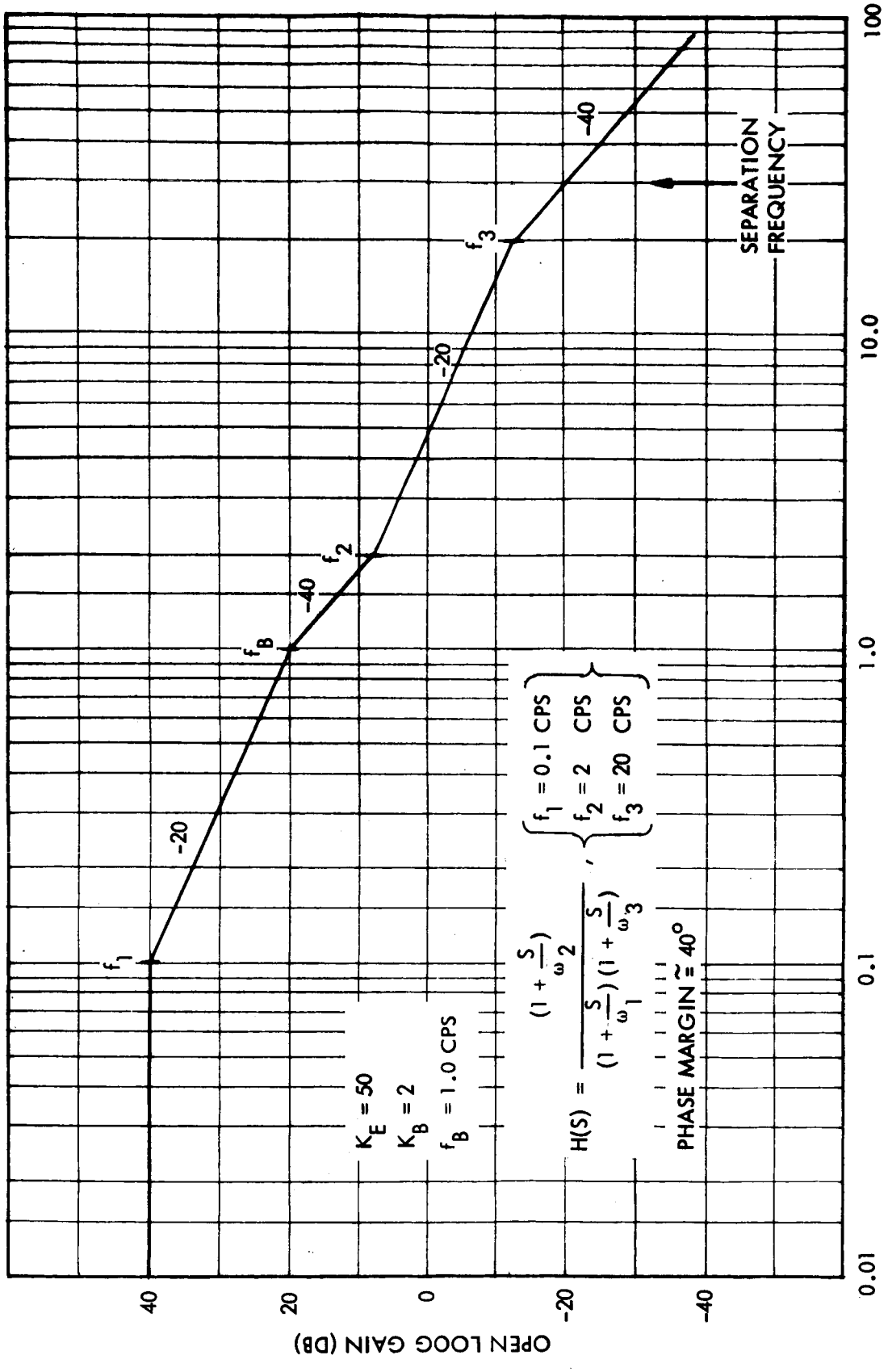

Figure 7. Bode Diagram for Amplitude Control Loop

Section 4

GYRO INVESTIGATIONS

The following pages describe the contract effort relating to the problem of null instability of the rate sensor output signal. Each of the principal development areas (beams, crystals, bonding, mounts and leads) are discussed.

BEAMS

SIZE

It was recognized at the start of this contract that the then existent two-inch beam length was complicating a separation of the problem areas associated with the solid state rate sensor. Previous tests were conducted on both five and two-inch beams. These tests indicated that better and more consistent results were achieved with the longer beams.

While it was evident that a longer beam would enable the isolation of problem areas more readily, it was not felt necessary to go to a five-inch length. Rather, it was decided that a beam with a resonant frequency of not less than 1500 cycles/second would be a good compromise. This resulted in the selection of a beam four inches long. The advantages of the longer beam are:

1) The mounts become less critical.

2) The piezoelectric crystals have less influence in determining the rate sensor's characteristics. (The crystals are the same size as were those used with the two-inch beam, but now cover only about one-third of the distance between the nodes.)

3) The leads are less critical. They have the same mass and length and thus, they are proportionately less effective in influencing the sensor.

4) The signal levels are improved. For a given drive voltage, the amplitude of the vibration and the resultant signal output are much higher with the four-inch beam.

While the four-inch beam offers definite advantages, there is a resultant disadvantage. This arises because the bandwidth is essentially equal to the separation of the resonant frequencies of the drive plane and the readout plane (see Section 3 on frequency separation). Since the resonant frequency is inversely proportional to the square of the length of the

beam, and the frequency separation of the drive plane and readout planes is determined by decoupling considerations, the bandwidth is reduced considerably in a four-inch beam as compared with a two-inch beam.

With these considerations as basis, the change was made to the four-inch length. Subsequent tests confirmed the anticipated results and the larger size has allowed a better definition of problem sources and enabled pursuit of their solutions in a logical manner.

While the four-inch length is desirable at this stage of the development program, it is felt that once the problem sources are isolated and minimized in the four-inch size, the reduction to a two-inch beam length will be straightforward.

MATERIALS

Stainless Steel

Early solid state gyro beams were fabricated with type 303 stainless steel. This material had the advantages of immediate availability, easy machinability, and a high mechanical quality factor (Q). It had the disadvantage of having a very high coefficient of linear expansion (16.5×10^{-6} in/in/C^{o} for the stainless steel as compared with 4.5×10^{-6} in/in/C^{o} for the piezoelectric crystals). Because of this mismatch, other materials were sought which more nearly matched the expansion characteristics of the crystals. Two materials were found which satisfied this criterion. They were molybdenum and Ni-Span C.

Molybdenum

The molybdenum has a coefficient of linear expansion of 5.7×10^{-6} in/in/C^{o}. From this standpoint, it would be excellent. However, it has the disadvantage that the mechanical stability of the material varies with time. A second disadvantage is that special tooling and machining is required which makes fabrication of test beams difficult.

Ni-Span C

The Ni-Span C material is a nickel, chromium, titanium alloy which has a very high mechanical quality factor (2000 in annealed state, and as high as 8000 in the cold worked condition). Its coefficient of linear expansion ranges from 3.2×10^{-6} inches/inch/C^{o} for the alloy with no titanium to 7.5×10^{-6} inches/inch/C^{o} for the standard titanium alloy. The addition of titanium allows a heat treatment process to obtain a zero value for the thermoelastic coefficient (i.e., Young's modulus is temperature independent).

Beams were fabricated with this material and operation was quite satisfactory. The mechanical quality factor (Q) was over 700, and machining was relatively straightforward. This material was chosen and subsequently used for all beams.

CRYSTALS

The piezoelectric crystals used on the solid-state rate sensors have been purchased from the Clevite Corporation. They are commercial versions of lead titanate zirconate. These ceramics have the advantages of a strong piezoelectric effect and a high Curie point.

The two specific ceramics used during this contract were PZT-4 and PZT-7A. The former is a standard production crystal and the latter is a new material available from the Electronic Research Division of the Clevite Corporation. The PZT-7A has a higher g_{31} constant (open circuit gain constant) and is specified as having a constant voltage output with temperature when connected in parallel with an appropriate capacitor. The coefficient of linear expansion of these crystals is 4.5×10^{-6} inches/inch/C^{o}.

With the use of the high impedance buffer amplifiers described in the electronic section of this report there is a definite advantage in using PZT-4 rather than PZT-7A crystals for driving and readout of the rate sensor. While the thermal stability of the PZT-7A crystal is superior to that of the PZT-4, it has a much lower capacitance (approximately 400 mmfds as compared to 1200 mmfds for the PZT-4). This results in a much higher output impedance for the PZT-7A crystals and would require buffer amplifiers with input impedances on the order of 15 megohms to eliminate significant loading effects.

Since such input impedances are difficult to obtain, the PZT-4 crystals were utilized. Recent tests have indicated, however, that low impendence readout buffer amplifiers can be used with the piezoelectric cyrstals providing a current rather then voltage type readout. Hence, the PZT-7A crystals could be used and might provide better temperature stability.

BONDING

Extensive effort was expended on this contract to develop a satisfactory technique to bond the piezoelectric crystals to the Ni-Span C beam. At the start of the program this bond was made using a conductive epoxy (Hysol No. 4238). While a satisfactory bond could be achieved at room temperature, it was found that the transmissibility of the epoxy dropped off severely above 80^{o}C and started to deteriorate as low as 40^{o}C. This resulted in a significant decrease in feedback voltage with increasing

temperature and large null shifts. The transmissibility factor was found to be simply the Youngs modulus of the bonding material. The requirement is that Young's modulus remains constant over the temperature range.

After extensive effort was applied with various high temperature epoxies, glues, low temperature solders and brazing, a satisfactory bond was achieved using a silver doped indium solder. This solder bonds through the fired-on silver electrode directly to the crystal and provides significantly better transmissibility characteristics and excellent bond strength. This bonding technique was used on all subsequent gyro tests and on the two final units. It is believed to have been a significant break through and advancement of the state-of-the-art of crystal bonding especially where large size crystals are concerned.

MOUNTS

In the earlier months of this contract and on previous Company development programs the solid state gyro beams had been mounted at their fundamental resonant nodes with rubber diaphrams. These had a square hole cut in them and were slipped into grooves machined around the beam at its nodal points. While this approach worked satisfactorily, it was objectionable from the standpoint that the grooves cut in the beam reduced the effective cross section. Other mounts had been used on beams without grooves, but it was difficult to obtain a uniform fit to the beam or to secure these to the beam.

This diaphram mounting technique was improved by the casting of silicon rubber diaphrams (RTV-60) about the beams. This provided a mount which was a precise fit to the beam, and was bonded directly to the beam. However, even with this improvement, it was recognized that a significantly better mount must be developed to support the beam at its nodes if null stability was to be achieved with time, temperature, and shock variations.

The diaphram mount was felt to have inherent limitations. It made assembly difficult and prevented achievement of consistent and satisfactory results over the environmental range.

Extensive tests were then made of various mounts, and a simple 0-ring design was developed. This mount indicated a definite improvement in null stability with temperature variations and time. It also provided a simplified fabrication and assembly of the beam and a higher mechanical quality factor.

This mount required a new design of the beam. The beam is now designed with a rectangular central section and a cylindrical cross section located from the fundamental frequency nodes out to the beam ends. See Figure 13 in Section 6.

ELECTRICAL LEADS

An area which was found to be of considerable significance from the standpoint of short term stability was the placement and length of the wire leads to the piezoelectric crystals.

Testing indicated that these leads would frequently oscillate, or vibrate in a random manner. The result was to produce erratic variations in the output signal.

A satisfactory solution was achieved by attaching the leads to the beam and bringing them away from the beam at its nodal points. This was accomplished by using a formex varnish to glue the leads to the beam. They were then dressed one on each side of the beam out to the silicone 0-rings and up away from the beam. (The wire used for the leads is No. 43 heavy formex.) Figure 8 shows the sensor support structure and the location of the beam, leads, O-ring mount and crystals.

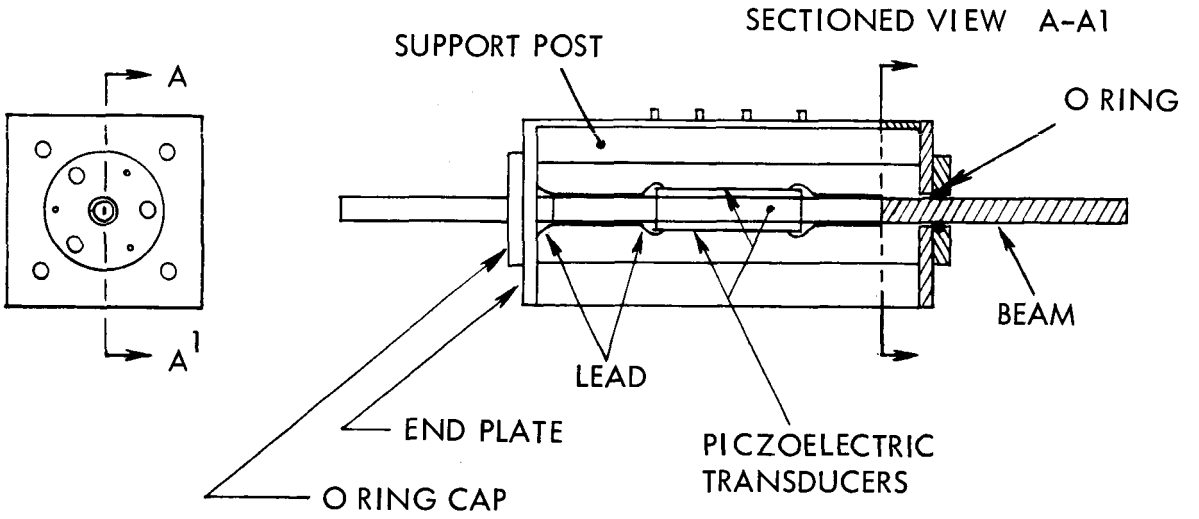

Figure 8. Sensor Support Structure

Section 5

ELECTRONICS

MICROELECTRONICS CIRCUITS

The recent advances of microelectronics technology has made operational amplifiers feasible as analog circuit building blocks. The electronics used in the solid state gyro employs the versatile properties of the μA709C, a microelectronic operational amplifier. The manufacturer's specifications of the μA709C are located in Appendix A.

The advantages of using these amplifiers, besides that of overall size, are many. They can provide high input impedance with gain, very high voltage gains whose outputs appear as voltage sources, eliminate large coupling and bypass capacitors required with conventional circuitry, and eliminate the transformer in the demodulator. One disadvantage results; a plus and minus power supply is required. This, however, also helps to eliminate large dc bias on the transducer crystals.

The amplifiers are used primarily in three configurations: an inverting voltage amplifier, a non-inverting voltage amplifier, and in the case of the low impedance readout circuitry, an inverting transimpedance amplifier (current to voltage).

The three configurations are shown in Figure 9 a, b, and c with their approximate loop gain transfer functions and impedance levels. The gain levels are set by external resistors, and frequency compensation is provided by capacitor and resistor networks as specified by the manufacturer's data sheet. The gain setting resistors are all 1/8 watt, one percent tolerance; trim pots are one watt, five percent; and the compensation components are 1/4 watt, five percent tolerance.

The two specific functions of the gyro electronics, beam drive and readout, are physically laid out on separate circuit boards and shown in Figures 10 and 12. The readout buffers for the two units are not identical. To eliminate noise and stray capacity problems associated with high impedance circuits, a set of low impedance buffers (transimpedance) are used in the readout of unit No. 1. This will allow a comparison with the high impedance circuits of unit No. 2

READOUT CIRCUITRY

The readout circuits are shown in Figure 10 for the high impedance buffers of unit No. 2 and in Figure 11 for the low impedance buffers of unit No. 1. The high impedance buffer function of the readout circuitry uses two

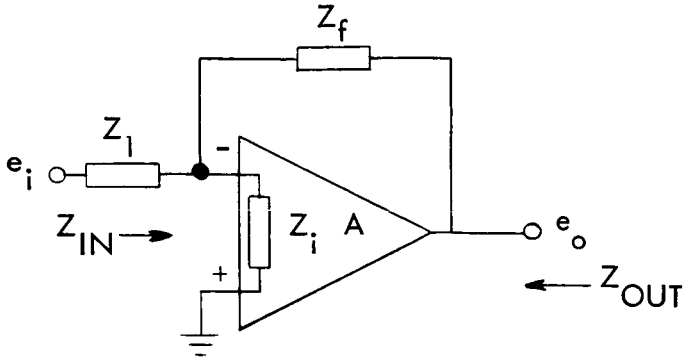

$$\frac{e_o}{e_i} \cong -\frac{Z_f}{Z_1}$$

$$Z_{IN} \cong Z_i$$

$$Z_{OUT} \cong 0\ \pi$$

INVERTING VOLTAGE AMPLIFIER

(a)

A ≡ OPEN LOOP GAIN OF OPERATIONAL AMPLIFIER

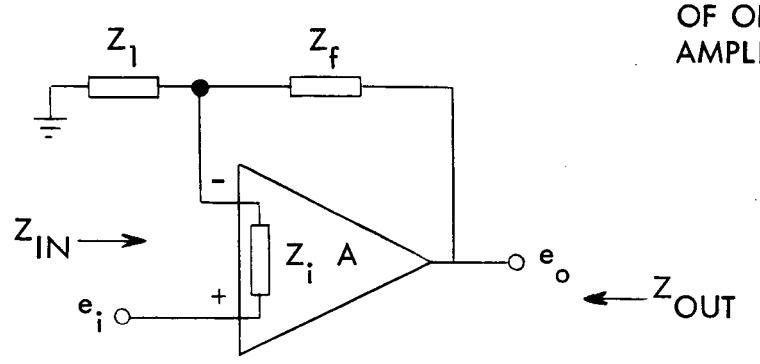

$$\frac{e_o}{e_i} \cong \frac{Z_1 + Z_f}{Z_1}$$

$$Z_{IN} \cong A\ Z_i$$

$$Z_{OUT} \cong 0$$

NON-INVERTING VOLTAGE AMPLIFIER

(b)

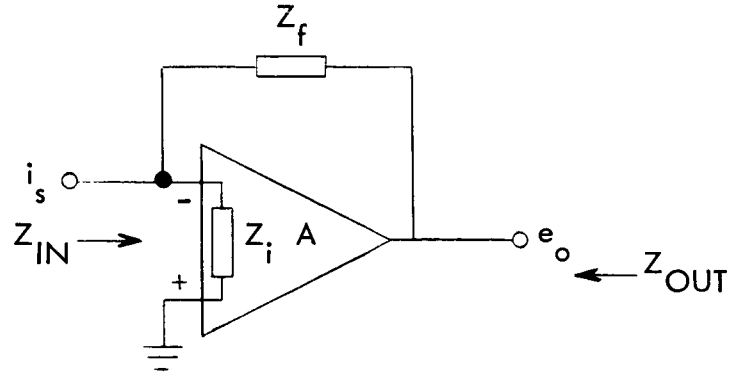

$$\frac{e_o}{i_s} \cong -Z_f$$

$$Z_{IN} \cong \frac{\frac{Z_f Z_i}{Z_f + Z_i}}{A}$$

$$Z_{OUT} \cong 0\ \pi$$

INVERTING TRANSIMPEDANCE AMPLIFIER

(c)

Figure 9. Basic Configurations of Operational Amplifiers

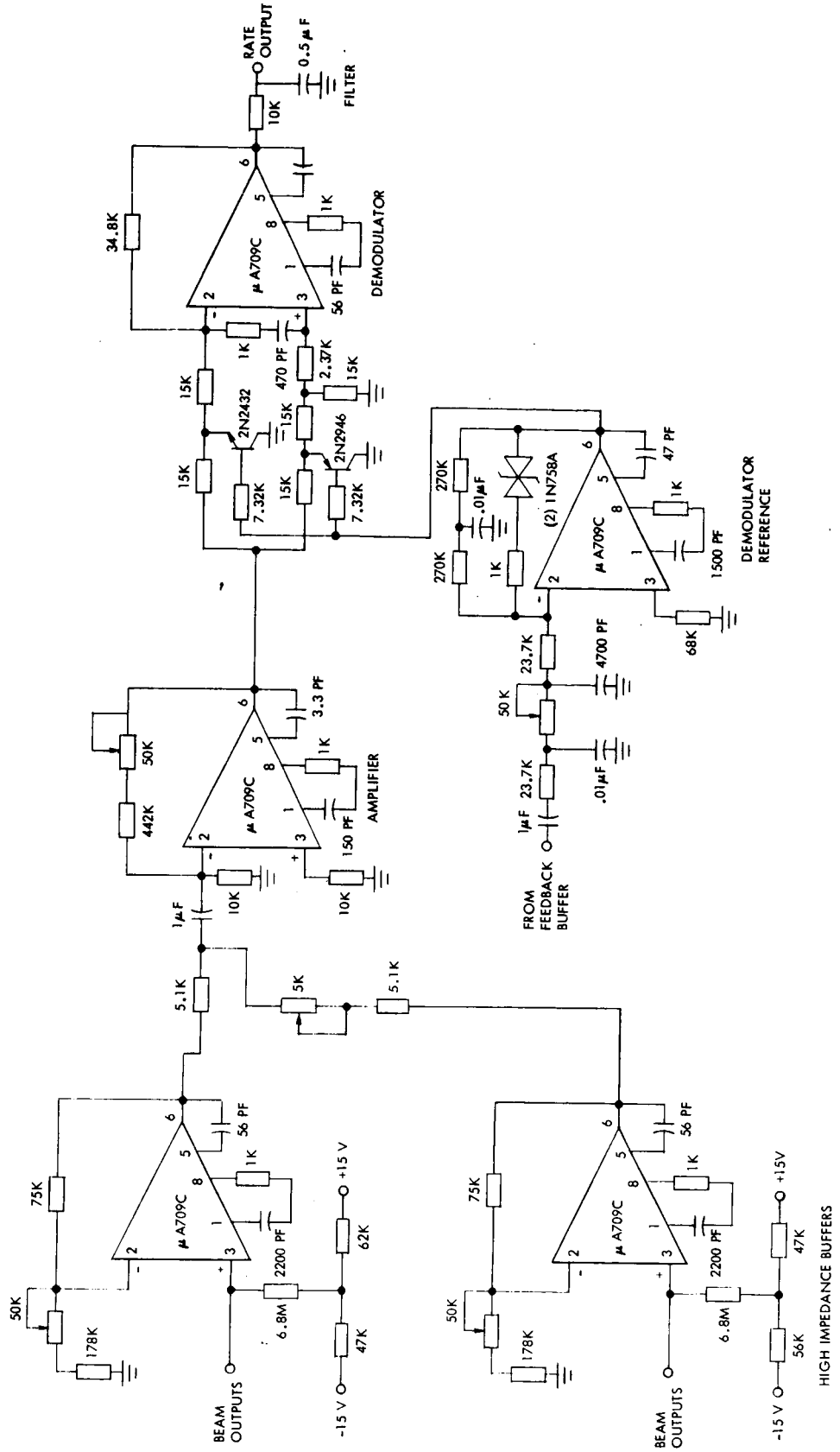

Figure 10. Beam Readout Circuitry - High Impedance Buffers

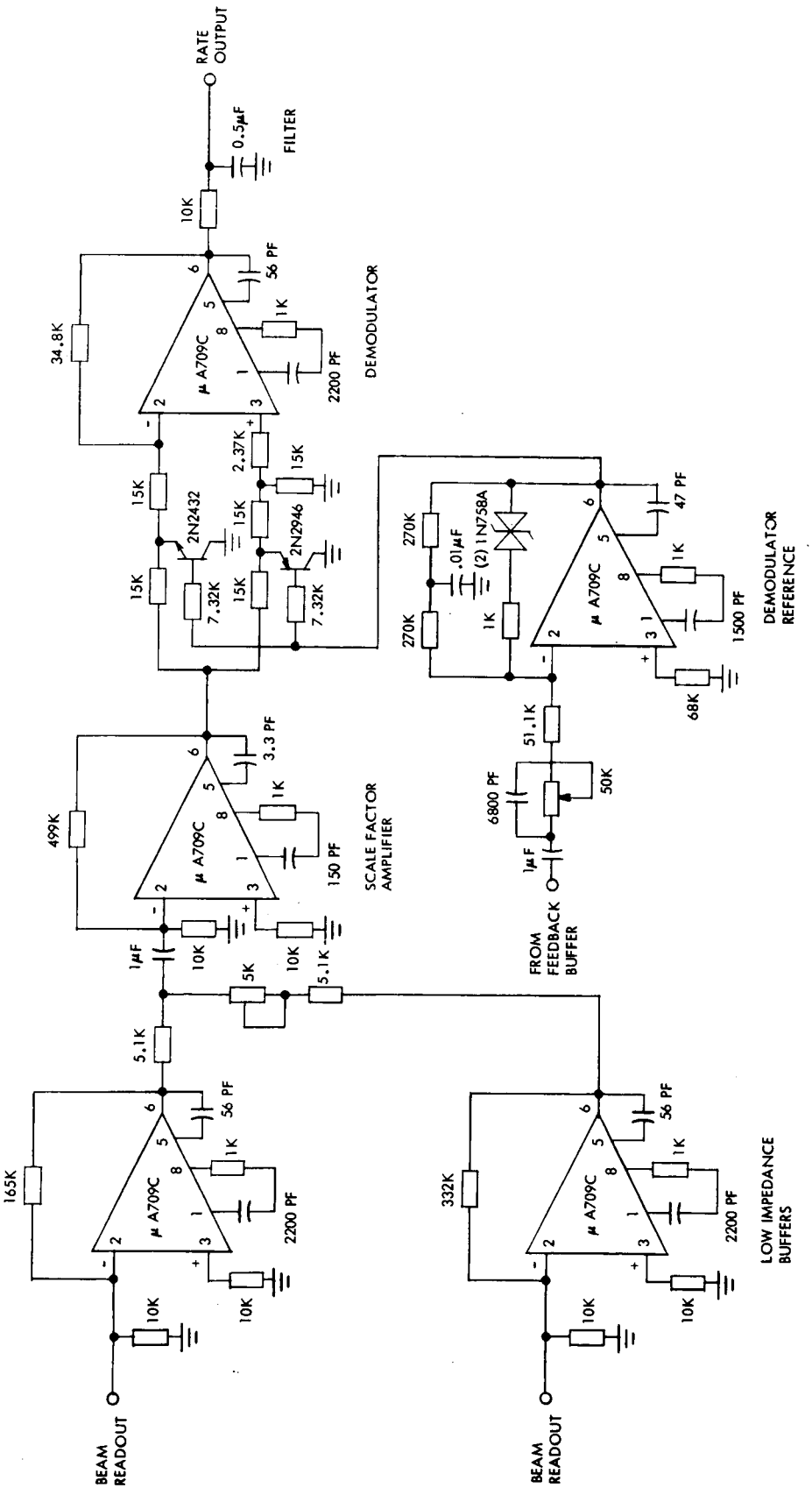

Figure 11. Beam Readout Circuitry - Low Impedance Buffers

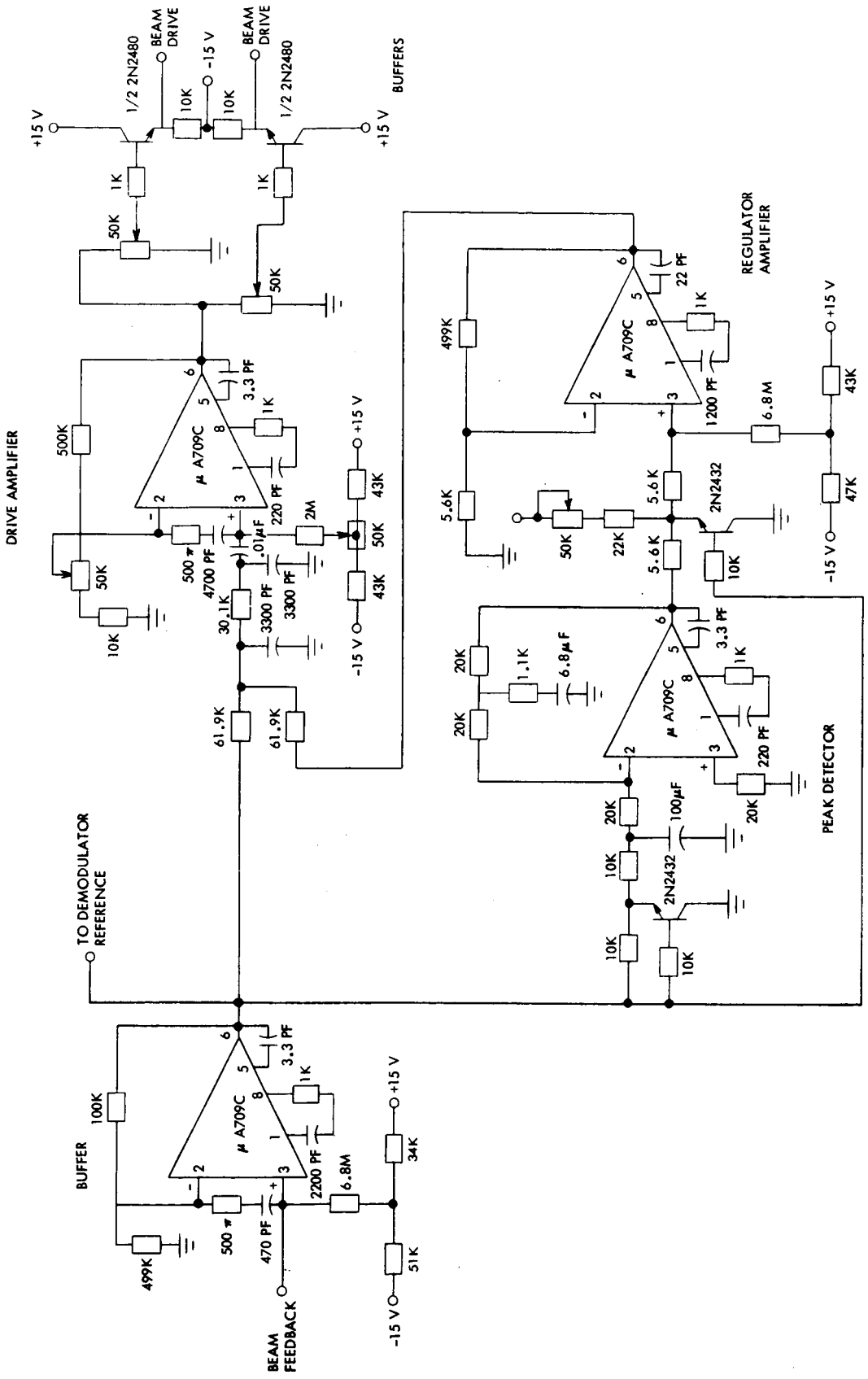

Figure 12. Beam Drive Circuitry

μA709's as non-inverting amplifiers. They are not used as voltage followers but have a gain slightly greater than unity with an effective input impedance of greater than 5 M ohms. A dc trimming network is required to insure the full ac range of the amplifier. Since both halves of the readout transducer do not have equal outputs of quadrature signal, the outputs are summed into the readout amplifier through different scaling resistors. A potentiometer adjustment of one scaling resistor value provides quadrature null control. The high gain readout amplifier is capacitor coupled to the buffers to prevent any slight dc offset from being amplified.

The phase null is minimized by adjustment of the drive amplifier's buffers. The null voltage is primarily third harmonic introduced by the regulator circuitry.

The low impedance buffer configuration uses two μA709's as inverting transimpedance amplifiers. Since a current readout of the transducer is now employed, the readout signal is nearly in phase with the feedback voltage. This necessitates changing the phase shift network to the demodulator reference to make it compatible with the signal.

The readout amplifier is a μA709 used as an inverting amplifier. The amplifier's gain is fixed, depending on the scale factor required. By changing the feedback resistor (Z_f), the gain can be easily adjusted for low or high rates.

The high gain of this amplifier also increases the null voltage. Fortunately, the null voltage is in quadrature with the rate signal voltage and is not passed by the demodulator.

The demodulator employs a μA709 with a pair of complementary chopper switches. The amplifier is used alternately as an inverting and noninverting amplifier with equal gain in either mode. The ac rate signal is then a positive full wave rectified signal if it is in phase with the demodulator reference drive. When the signal is 180 degrees out of phase with the reference, a negative full wave rectified signal appears. Therefore, rates in opposite directions are indicated by the polarity out of the demodulator. A 10 K output resistor is provided from the demodulator. A 0.5 μf capacitor to ground provides filtering.

The use of complementary chopper transistor switches eliminates the need for a 0 degree and 180 degrees reference. The chopper drive uses another μA709 which is used as a high-gain inverting amplifier zener limited to keep it out of saturation. This minimized the deadband of the switching transistor, since the output of the amplifier is now a reasonably square wave drive. The feedback voltage of the driver circuitry must be phase shifted by a passive filter prior to amplification. The trim pot allows adjustment for

best null on the quadrature signal out of the demodulator. Both high impendance and low impedance buffer configurations require phase shifting, but use different methods as shown in Figures 10 and 11.

BEAM DRIVE CIRCUITRY

The beam drive circuitry, refer to Figure 12, employs a μA709 buffer identical to those used in the high impedance readout. Besides offering a high impedance to the feedback transducer, it provides drive for the demodulator reference and the regulator.

The function of the regulator is to maintain a constant beam amplitude through monitoring the feedback voltage. This is done by half-wave peak detecting the feedback, comparing it to a reference, amplifying the error signal, and summing it with the feedback voltage into the drive amplifier.

The half-wave peak detector of the regulator uses a μA709 as an inverting amplifier. A chopping transistor switch provides a negative half wave rectified feedback voltage to the peak detector. The peak detector output offers a positive dc which is summed with a negative reference dc at another chopper transistor point. When the negative reference is nulled with the peak detector output, the feedback voltage is set at a nominal 10 volts peak to peak. This null point is capacitively connected to another μA709 noninverting high gain amplifier which senses any deviation from null. If the feedback voltage tends to drop, a negative error signal will develop and the regulator will add a square wave in phase with the feedback into the drive amplifier. This will increase the drive voltage applied to the beam, and hence, drive the feedback up to its nominal level. Similarly, an increase in feedback voltage will develop a positive error signal and add an out-of-phase square wave to the feedback voltage, thus decreasing the drive voltage and the feedback voltage. The square wave error signal is caused by the chopping action at the null point. The nominal feedback voltage can be adjusted by the negative reference trim pot.

The driver amplifier is a μA709 used as a noninverting amplifier with adjustable gain. It sums the error signal with the feedback signal and provides drive to the output buffers.

The output buffers are two adjustable emitter followers, each driving one half of the drive transducer. Unequal drive signals on each half of the transducer are required to minimize phase shift in the in-phase signal appearing in the readout circuitry.

Section 6

GYRO DESIGN AND PACKAGING

SENSOR UNIT

The sensor unit has been designed to provide reasonable decoupling of the input and output planes while providing adequate rate sensitivity. The original design computations are presented below.

The fundamental vibrational frequency of the beam was found from the formula

$$f_1 = \frac{\alpha_1 h}{2\pi \ell^2} \sqrt{\frac{EG}{12\rho}} \tag{9}$$

where

$$\alpha_1 = 22, \quad E = 4.03 \times 10^9 \text{ lb/ft}^2; \quad \rho = 510 \text{ lbs/ft}^3;$$

$$\ell = .33 \text{ ft}; \quad h = 1.04 \times 10^{-2} \text{ ft}$$

substitution of these values indicated that the vibrational frequency would be approximately 1500 cps.

The calculated value was somewhat lower than had been obtained on actual units. Due to the mass of the Piezoelectric crystals mounted on the beam and the rounded cross section of the ends of the beam, the actual vibrational frequency was expected to be approximately 1675 cps.

It was assumed that the input and output planes should be decoupled to 1.25 degrees phase overlap. This allowed the required frequency spread of the drive and readout planes to be found from equation (6) in Section 3.

$$f_o - f_c \approx \frac{f_o}{2\phi_o Q_o} \tag{10}$$

$$\phi = 1.25^o = 2.2 \times 10^{-2} \text{ radians}$$

based on previous empirical results $Q_o \approx 720$.

hence:

$$f_o - f_c \approx \frac{1675}{2(720)\,(2.2 \times 10^{-2})}$$

or $$f_o - f_c \approx 53 \text{ cps}$$

Then using equation (9), the actual beam dimensions were determined.

From equation (9), $f_c = h_c K$

where K is some constant; assume $h_c = .127"$

$$K = \frac{f_c}{h_c} = \frac{1675}{.127} \approx 13150$$

To obtain a given frequency separation we used this value of K and solved for h_2. However, since we were not dealing with a uniform cross section beam, an empirical compensation factor had to be introduced. Based on results obtained with a prior three inch beam, this factor was 1.6.

Thus

$$h_o = \left[f_c + 1.6\,(f_o - f_c) \right] \Big/ K$$

$$h_o = \left[1675 + 1.6(50)\right] \Big/ 13150$$

$$h_o = .133"$$

The beam dimensions had now been determined and the result is shown in Figure 13.

The design of the electronics has already been covered in the previous section, so no further discussion will be given here.

PACKAGE

Figure 14 shows a full size layout of the gyro package containing both the sensor and the electronics. The two parts of the fixture can be separated allowing remote location of the electronics where space or weight is important.

No effort has been made to minimize the size or weight of the package, or of the sensor and electronics. These could both be reduced by a factor of four or five with nominal effort.

The present package is designed to allow straightforward fabrication and assembly of the gyro, and to allow for convenient testing and making of adjustments. It provides ready access to all parts of the electronics or of the sensor unit, and provides a rigid mount for the gyro.

Figures 15 and 16 are photographs of the final breadboard unit.

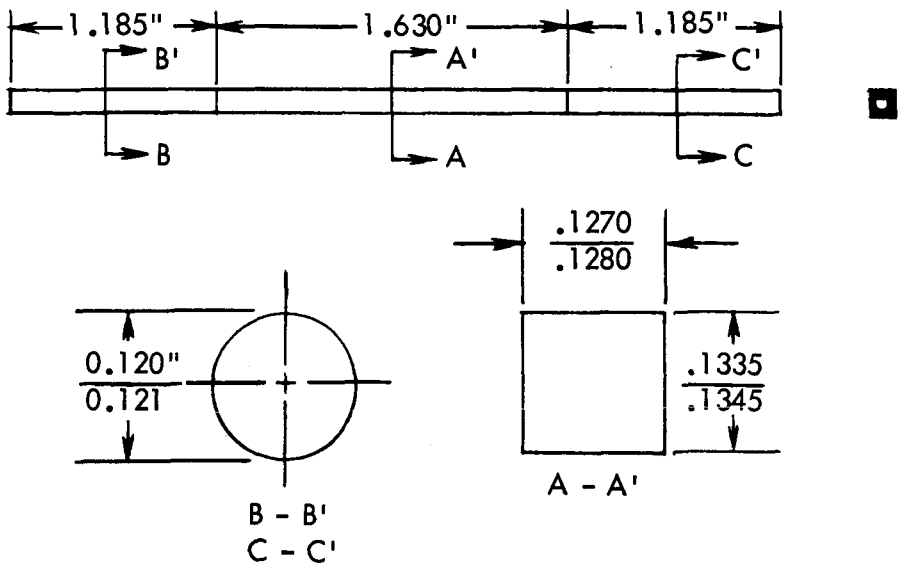

Figure 13. Beam Design and Dimensions

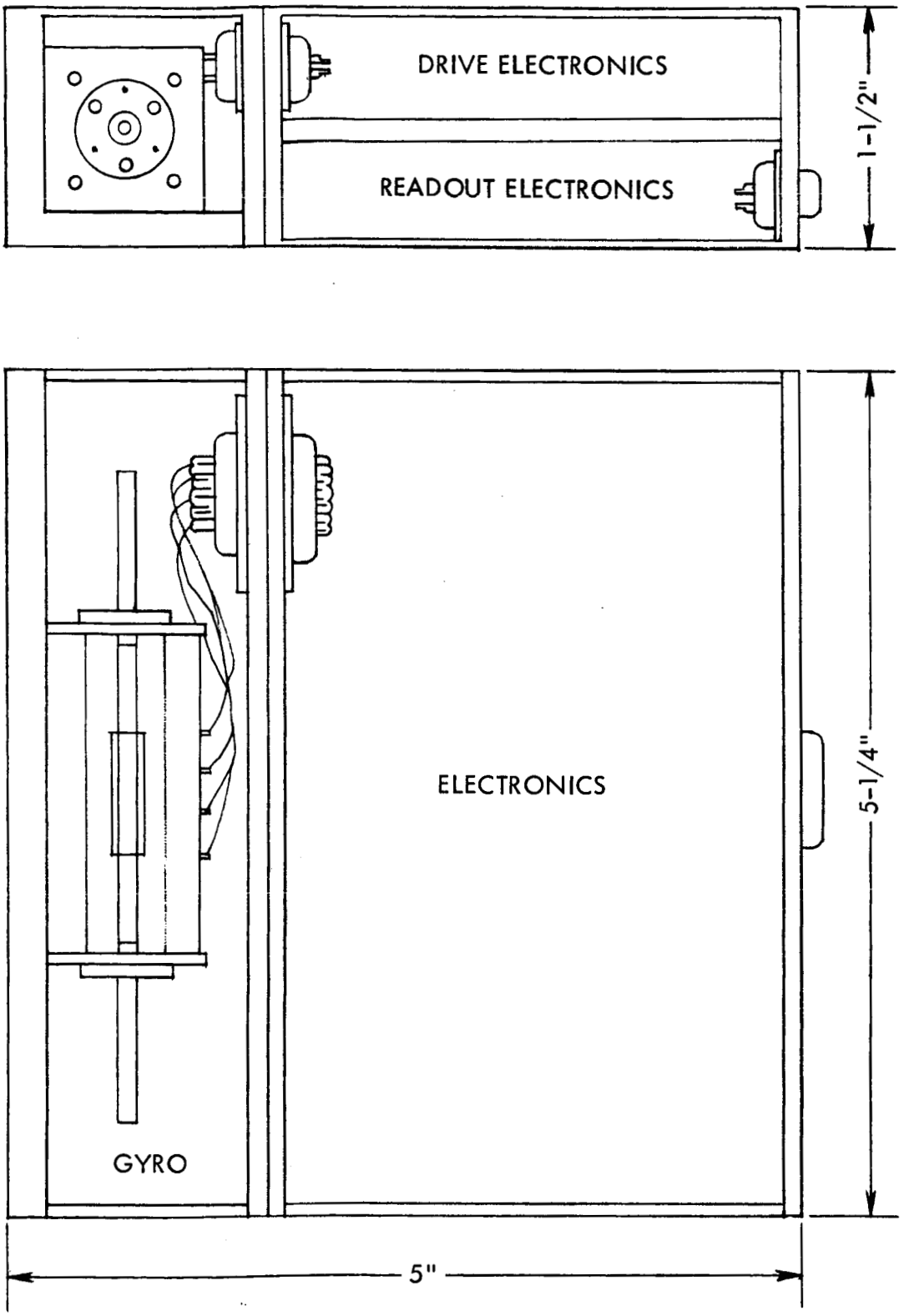

Figure 14. Solid State Rate Sensor Package

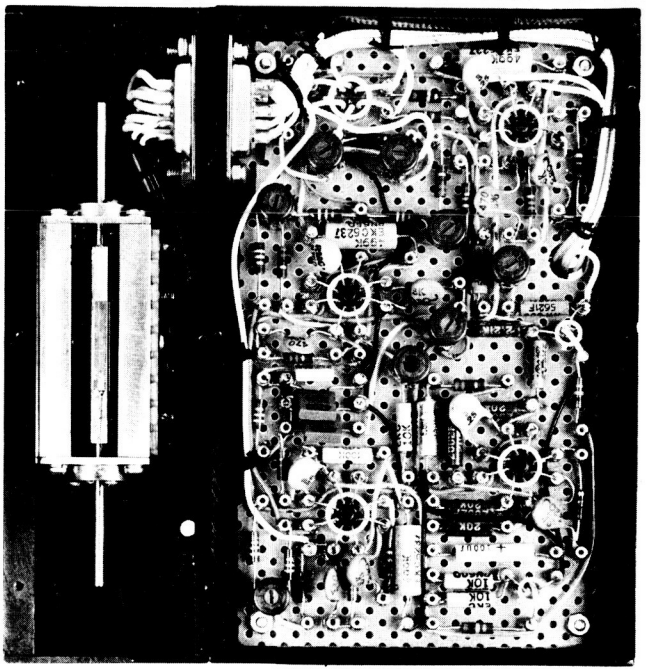

Figure 15. Photograph of Rate Sensor and Electronics Assembly

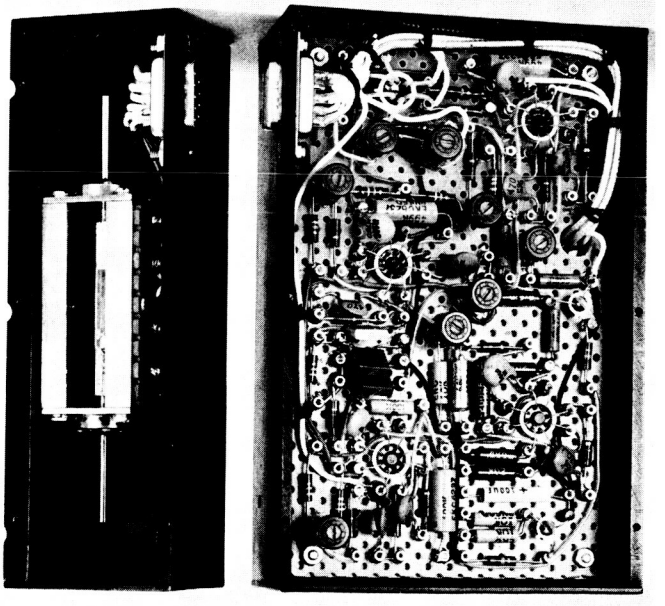

Figure 16. Photograph of Rate Sensor and Electronics Units

Section 7

TESTS

INTRODUCTION

During the last two months of the present phase of the contract, extensive testing of the two rate sensor assemblies has been conducted. Tests have been run to determine threshold, hysteresis, linearity, scale factor, scale factor change with temperature, frequency response, damping ratio, cross coupling, "G" sensitivity, power, start up time, long term drift, and null shifts with temperature. The test results are discussed in the following paragraphs. In general, the results have been very promising.

As the following pages will show, significant advancements in the state-of-the-art of solid state rate sensors have been achieved.

Table 1 summarizes the test results and presents a comparison of the present sensor performance with the long-range design goals and with the sensors characteristics at the start of the present contract. The long-range design goals were established at a meeting held in Johnson City, New York with the NASA/ERC project engineer on July 15, 1965, and were presented in monthly report No. 1

As can be seen from this table, significant advancements have been made in the sensor performance during this contract and many of the long-range design goals have been met. At this stage of the sensor development there are three development areas which require further effort. Two of these, the drift with temperature and the frequency response, have been recognized as significant problem areas for some time. The third area however, "G" sensitivity, has just been recognized during the test phase of the present programs. Another area requiring further effort but primarily from the quality control aspect is that of obtaining uniformity in crystal beam bonding.

GENERAL TESTS

The following paragraphs present a detailed discussion of the tests and the test results.

BEAM CHARACTERISTICS

Tests were conducted with two beams and two sets of electronics. The beams were designed to be similar in all of their characteristics. Table 2 shows a comparison of the measured beam characteristics.

TABLE 1

		Start of Contract	Completion of Present Contract	Design Goals
1.	Threshold	$0.1^{o}/S$	$0.01^{o}/S$	$0.001\text{-}0.01^{o}/S$
2.	Linearity	5%	1% full scale	1% full scale
3.	Scale Factor (output)	0.010-0.020 $V/^{o}/S$	0.050-0.070 $V/^{o}/S$	0.02 $V/^{o}/S$
4.	Scale Factor Change with Temperature (0-100°C)	100%	10%	1%
5.	Dynamic Range	±3 V	±9 V	-----
6.	Short Term Drift	$0.2^{o}/S$	$0.02^{o}/S$	-----
7.	Long Term Drift	$0.3^{o}/S/hr.$	$0.02^{o}/S/hr.$	-----
8.	Null Uncertainity	-----	$0.4^{o}/S$	0.1 to $1^{o}/S$
9.	Frequency Response	-----	300 Rads/S	1000 Rads/S
10.	Temperature Drift (20°C-70°C)	Saturated Output ($200^{o}/S$ +)	$\approx \pm 5^{o}/S$	
11.	Temperature Range	-----	+20°C to +70°C	-20°C to +70°C
12.	Undamped Natural Frequency	-----	48 cps	-----
13.	Damping Ratio	-----	0.02-0.03	0.5-0.1
14.	Max. Angular Rate	$50\text{-}1300^{o}/S$[1]	$50\text{-}1300^{o}/S$[1]	$50\text{-}2000^{o}/S$
15.	Power	1 watt 28 V	1 watt ±14 V	0.5 watts 28 V
16.	Start Up Time	1-3 secs.	1-3 secs.	0.2 sec.
17.	Life	1 year +	1 year +	1 year +
18.	Hysteresis	threshold	threshold	0.02% full scale
19.	Cross Coupling	-----	0.1%	0.01 to 0.1%
20.	"G"Sensitivity	-----	$+0.1^{o}/S/G$ $-0.06^{o}/S/G^{2}$	$0.001^{o}/S/G^{2}$

[1] Limited by max. rate of available rate table.

TABLE 2

BEAM CHARACTERISTICS

	Beam No. 1	Beam No. 2
$F_{Res.}$ Drive Plane	1594.7	1581.7
$F_{Res.}$ Readout Plane	1642.2	1630.3
$F_{Res.}$ (Readout) - $F_{Res.}$ (Drive)	47.5	48.6
Q_{Mech} Drive Plane	839	510
Q_{Mech} Readout Plane	864.3	815
Gain Drive Plane	1.57	1.25
Gain Readout Plane	1.77	1.73

The differences apparent in Table 2 are the result of different crystal characteristics (both electrical and mechanical), variations in physical placements of the crystals on the beam, and variations in other mechanical areas such as pressure of the 0-ring mounts, nodal separation and lead dress. The two beams were machined, fabricated and assembled at different times and the piezoelectric crystals were obtained from two separate batches purchased from the Clevite Corporation. Thus, the above results are more indicative of the range of variation that might be expected on separately procured sensors rather than sensors fabricated simultaneously.

The low "Q" (mechanical quality factor) in the drive plane of beam No. 2 was not consistent with the "Q"s obtained in the other plane, or that obtained on other beams. However, operation of the sensor appeared satisfactory, and aside from a resoldering of crystal leads and a check of crystal capacitance no attempt was made to eliminate this variation.

In all of the following tests, except where specifically stated unit No. 1 is used with a set of electronics having low impedance readout buffer amplifiers. These low impedance electronics utilize the readout crystals as current sources rather than voltage sources, and result in a reduced sensitivity to lead capacitance and noise. Test results indicate that these electronics provide more satisfactory sensor operation than the high impedance electronics. This is particularly true from the standpoint of the occurrence of sporadic shifts in the rate sensor null output. The low impedance buffers have reduced significantly the effect of cabling and connectors on the rate sensor null stability and allow remote operation of the sensor from the electronics. Such operation is very marginal with the high impedance amplifiers due to their sensitivity to changes in lead capacitance. Because little was known or understood about low impedance operation of

the piezoelectric crystals at the start of the test phase of the contract unit No. 2 was left unchanged and tests on it were done with the high impedance readout amplifiers.

FREQUENCY RESPONSE AND DAMPING RATIO

Frequency response tests were conducted using a Micro Gee Oscillating Rate Table Model No. 64A which provides constant peak-rates over a frequency range of from 1 to 100 cycles/sec. The resultant frequency response curves are shown in Figure 17 and Figure 2 in Section 3.

These are normalized plots of the uncompensated frequency response of the rate sensor. These curves show clearly the resonant peaking of the sensor at the difference frequency of the drive and readout planes. They point up the extremely low damping inherent in the present sensor design. The damping ratio can be found from the equation:

$$M_p \approx \frac{1}{2\delta} \quad \text{or} \quad \delta \approx \frac{1}{2M_p}$$

where M_p = peak amplitude at resonance

δ = damping ratio

The measured peaking at resonance is 22.4 for beam No. 2 and 22.9 for beam No. 1 hence

$$\delta_2 = \frac{1}{2\,(22.4)} = .022 \qquad \delta_1 = \frac{1}{2\,(22.9)} = .022$$

This shows that the present system is considerably underdamped and highly sensitive to any vibration at the difference frequency of drive plane and readout plane ($\approx$ 48 cps). On an independent company funded program preliminary circuits have been fabricated and tests have been conducted which establish the feasibility of using the demodulated output of the readout crystal to develop a damping signal which is then applied to the spare crystal in the readout plane. It is believed that this will enable setting of the damping ratio to any desired value. The circuits and technique will be further developed and refined on the following phase of the present contract.

The occurrence of this resonant peaking is in agreement with theory and utilizing the equation derived in Section 3 very close agreement is found between the predicted amplitude of peaking and the measured value.

$$Q_i = Q_o \frac{\omega_o - \omega_c}{\omega_o} \quad \text{(equation 7)}$$

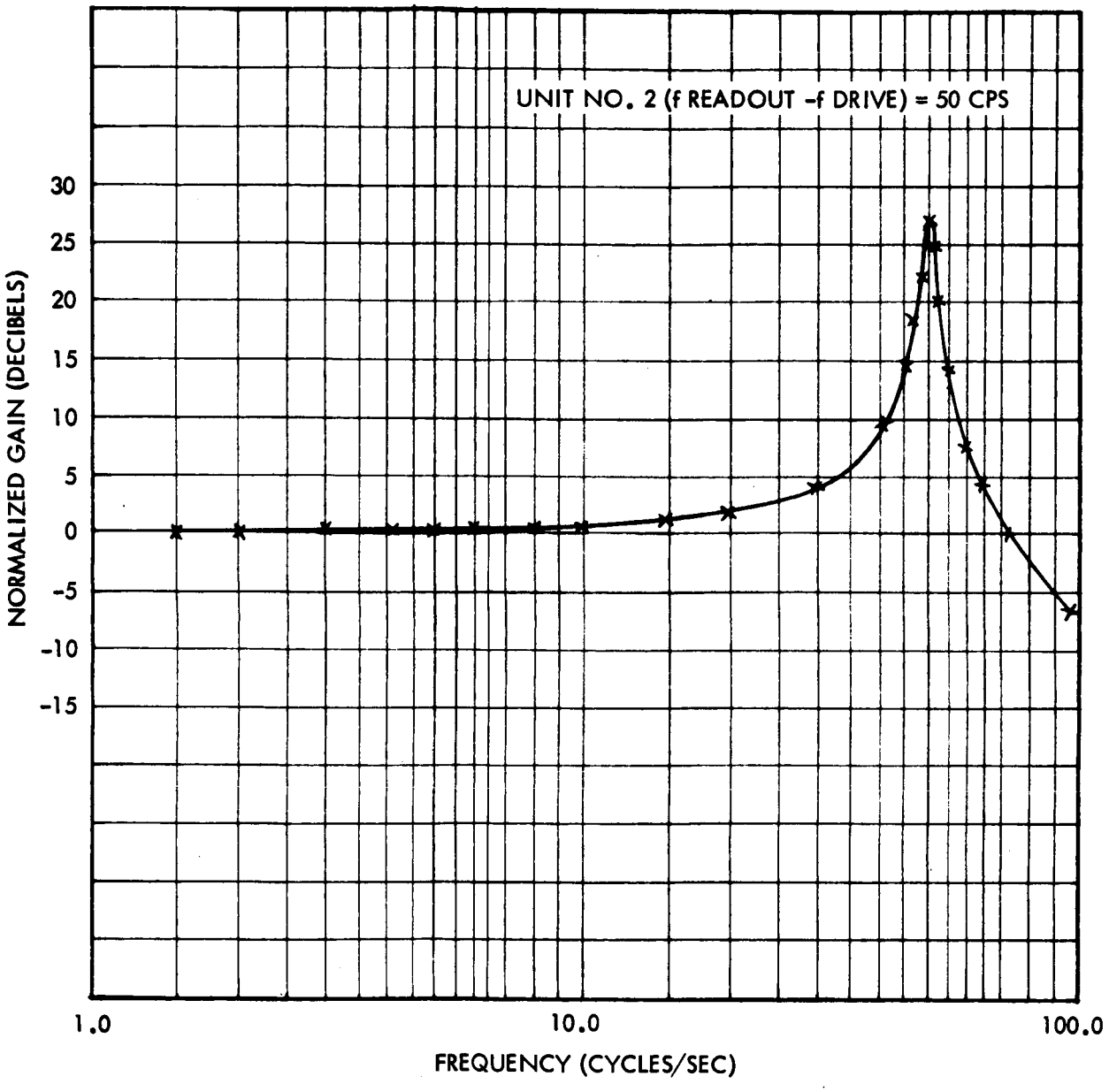

Figure 17. Frequency Response (Unit No. 2)

for beam No. 1

$$Q_i = 864 \frac{(1642.2 - 1594.7)}{1642.2} = 25.0$$

for beam No. 2

$$Q_i = 815 \frac{(1630.3 - 1581.7)}{1630.3} = 24.3$$

These are within 10% of the measured values of 22.9 for unit No. 1 and 22.4 for unit No. 2.

START UP TIME

The start up time of the solid state rate sensor can be varied by changing the gain of the drive amplifier. Figure 18 shows a measured characteristic of the turn on time – drive amplifier gain relationship. Turn-on is arbitrarily defined as the time required for short term transients of the demodulator output voltage to cease. The typical turn on time would be between 1 and 2 seconds.

POWER, SIZE AND WEIGHT

Measurements of power supplied to the two operating breadboard units were made with the results indicated below

Unit No. 1 total power = .86 watts

Unit No. 2 total power = .99 watts

These units were operating normally and were supplied from a ±15V dc laboratory power supply. The integrated circuits used have increased power by a factor of two over conventional circuitry. The plus and minus voltages also are required because of the use of integrated circuit operational amplifiers. These units allow simple design and modification of the electronic circuits, and are ideal for the development stages of the solid state gyro. The two units fabricated for this contract have a volume of 39.4 cubic inches including both the sensor and the electronics, and they weigh 1.8 pounds. As discussed previously, the package dimensions are 1 1/2" x 5 1/4" x 5". On a separate contract, units with the same beam and similar electronics have been designed and built with a volume of 15 cubic inches and a weight of approximately 14 ounces. This same sensor package could be reduced to 10 cubic inches and 8 ounces without undue difficulty.

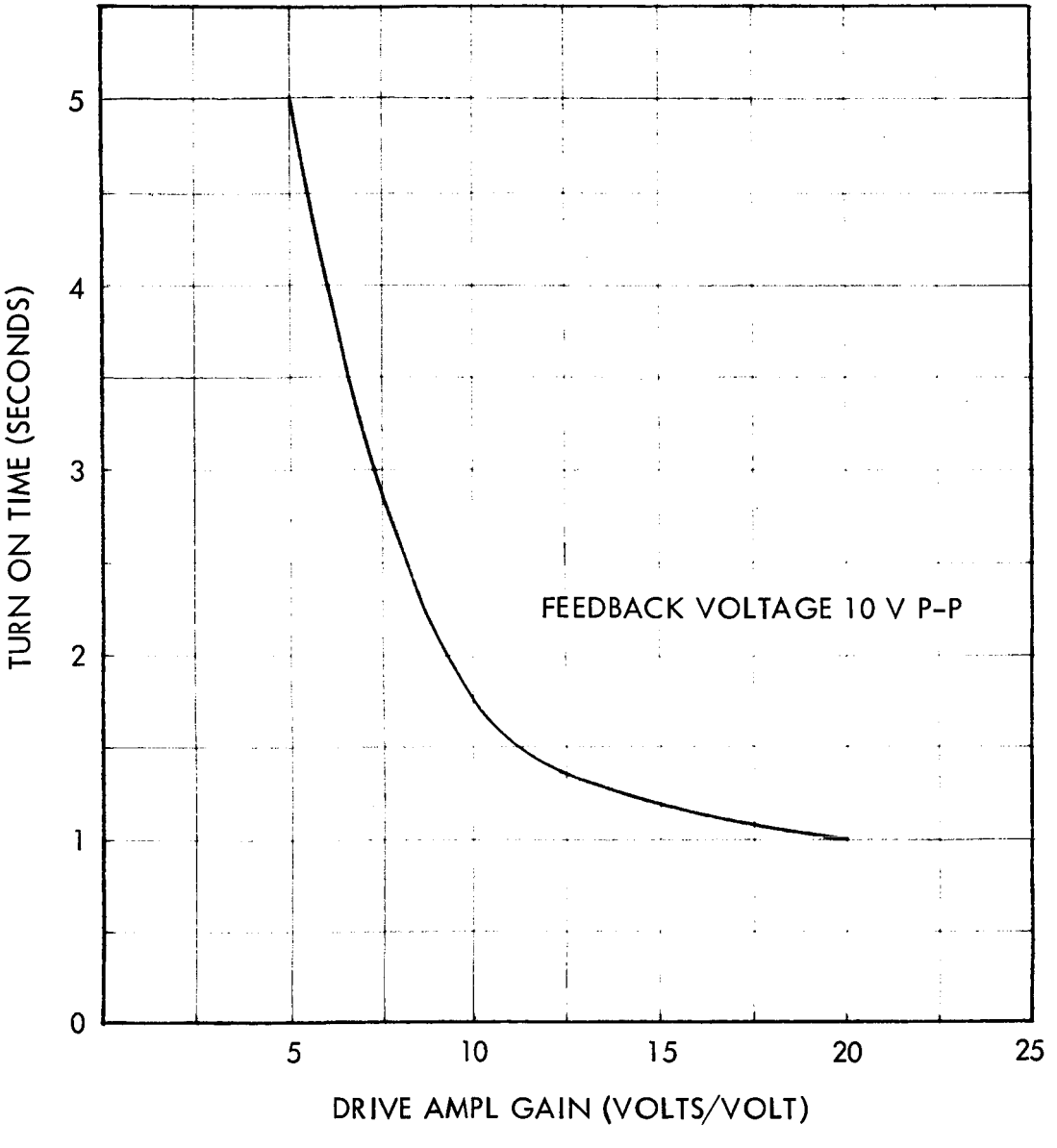

Figure 18. Turn on Time as Function of Drive Amplifier Gain

OPERATIONAL TESTS

THRESHOLD

Measurements indicate that the threshold of the present units is less than .01 deg/sec. This rate yields an output voltage somewhat less than the average peak-peak value of the short term null voltage variations.

Figure 19 shows these short term variations on the demodulator output of the solid state rate sensor as a function of time. On the horizontal scale two major divisions are equal to one second and on the vertical scale each major division corresponds to one millivolt. As can be seen, the average peak-peak null variations are about one millivolt which is, for this unit, equivalent to .015 deg/sec.

Figure 20 shows a similar trace where an input rate of .04 deg/sec has been applied at $t \approx 2$ seconds then removed at $t \approx 7$ seconds, a rate of .03 deg/sec applied at $t \approx 12$ seconds and this rate removed at $t \approx 16$ seconds. As is evident from this recorder trace, the amplitude difference between the .03 deg/sec and .04 deg/sec traces, which is $.01^{o}$/sec and the stated threshold, is easily distinguishable. Due to limitations of our present test equipment a trace could not be obtained for an input rate of less than .03 deg/sec.

A significant point which should be noted here is the coherent nature of the null voltage variations. There is a definite frequency component of approximately 2 cps predominant in the null signal. It is presently thought that this is related to the bandwidth of the electronic regulator, and future effort will be directed toward reducing or eliminating this coherent noise. This would result in a significant improvement in the present threshold which has already met the long term design goal of .01 deg/sec.

LINEARITY

Linearity tests were conducted on the two rate sensor units over the two full scale ranges, 0 to ±200 deg/sec and 0 to ±1200 deg/sec. These tests were run on a Genisco rate-of-turn table with a rate range of .01 to 1200 deg/sec. A magnetic pickoff driving a counter was used to obtain calibrated rate measurements at rates above 10 deg/sec. Rate measurements were made over a ten cycle average of the counter with ten sets of readings taken at each point. The rate sensor output voltage was averaged over the ten readings and the deviations from the calculated points were determined. These deviations are plotted in Figures 21 through 23 for the two full scale ranges. Figure 21 shows the results for a full-scale range of 200 deg/sec. Deviations in volts from the calculated linear plot are shown versus rate in degrees/second.

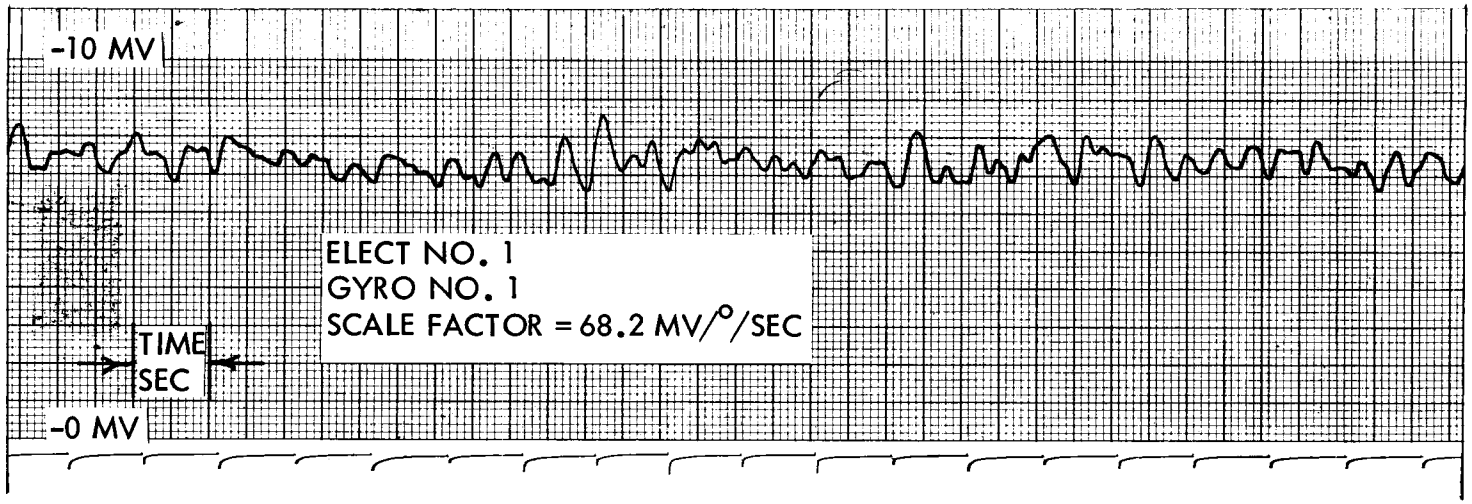

Figure 19. Recording of Demodulator Output

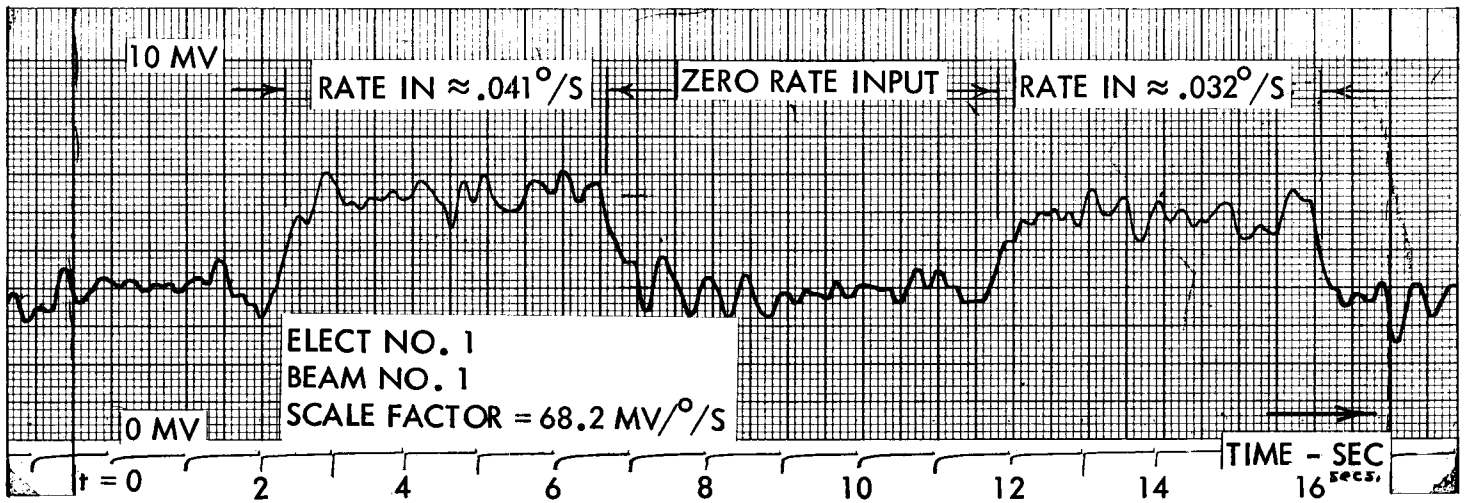

Figure 20. Recording of Sensor Threshold Measurements

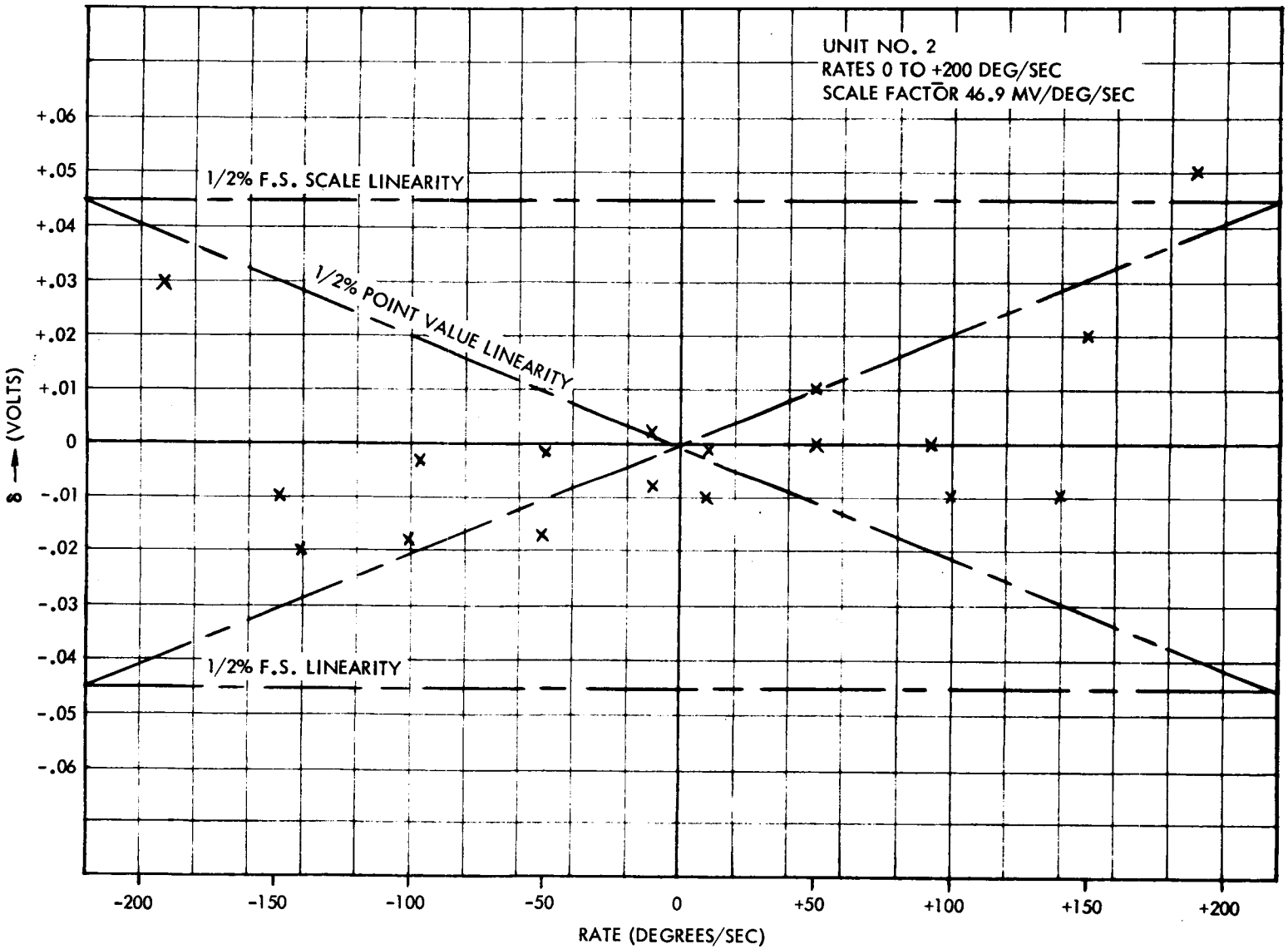

Figure 21. Linearity Deviations (Unit No. 2) 0 to ±200 Degs/Sec.

As can be seen in Figure 21 which is for unit No. 2 linearity is approximately 1/4% of full scale to 150 deg/sec and 1/2% full scale to 200 deg/sec. It should also be noted that with the exception of the region about the origin, where shifts of the zero null have occurred, linearity is within 1/2% of the actual measurement point value (the diagonal lines on the plot).

In Figures 22 and 23 similar plots are shown for a full scale range of the sensors of 1200 deg/sec. It should be noted here that linearity is better than one percent of full scale to beyond 1000 deg/sec, and that with the exception of the region about the origin, where null shifts have occurred after going to high rates and back down, linearity is on the order of one percent of the actual measurement point value.

HYSTERISIS

A series of tests were conducted to determine any hysterisis effects associated with the sensor output. Two rate loops (the first from 0 to +250 deg/sec to 0 to -250 deg/sec and back to 0, and the second from 0 to +1000 deg/sec to 0 to -1000 deg/sec and back to 0) were traversed ten times with measurements made at each of the above points. No hysteresis characteristics were observable although some null shifts which appeared to be random in nature were detected.

CROSS COUPLING

Tests were run to determine if any cross coupling of rate sensitivity existed in the solid state rate sensor. The unit was mounted so that its sensitive axis was perpendicular to the applied input rate axis. Shims were then used to minimize the output voltage for an applied rate. These shims were used to compensate for any mechanical misalignments or machining tolerances which might exist in the gyro mount, housing or test bed.

For unit No. 1, which had a scale factor of 72 mv/^{o}/sec at the time of this test, the following results were obtained:

Input Rate	Normalized Sensor Output
100 deg/sec C.C.W.	-4.4 M.V.
0 deg/sec	0 M.V.
100 deg/sec C.W.	+4.4 M.V.

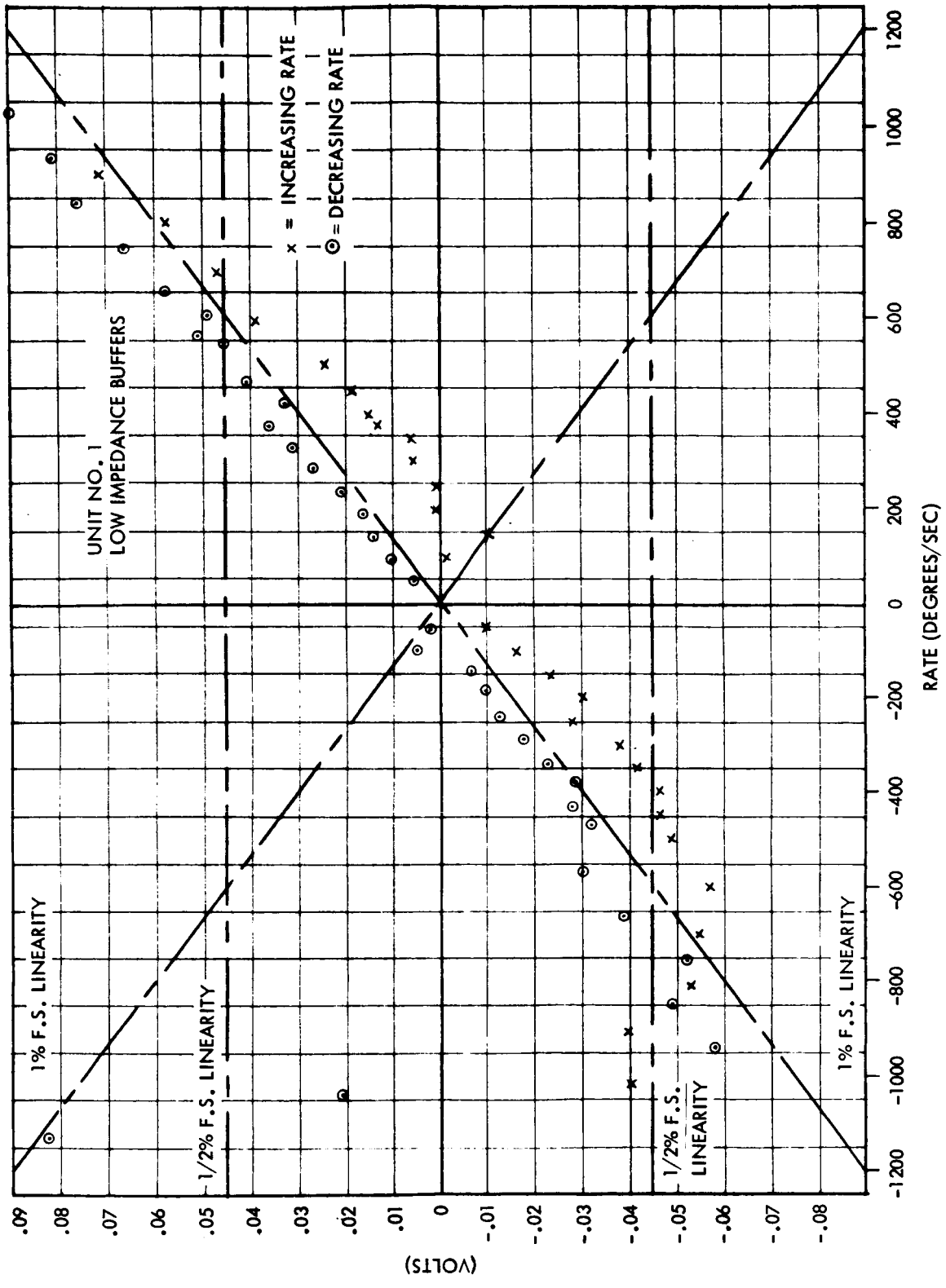

Figure 22. Linearity Deviations (Unit No. 1) 0 to ±1200 Degs/Sec.

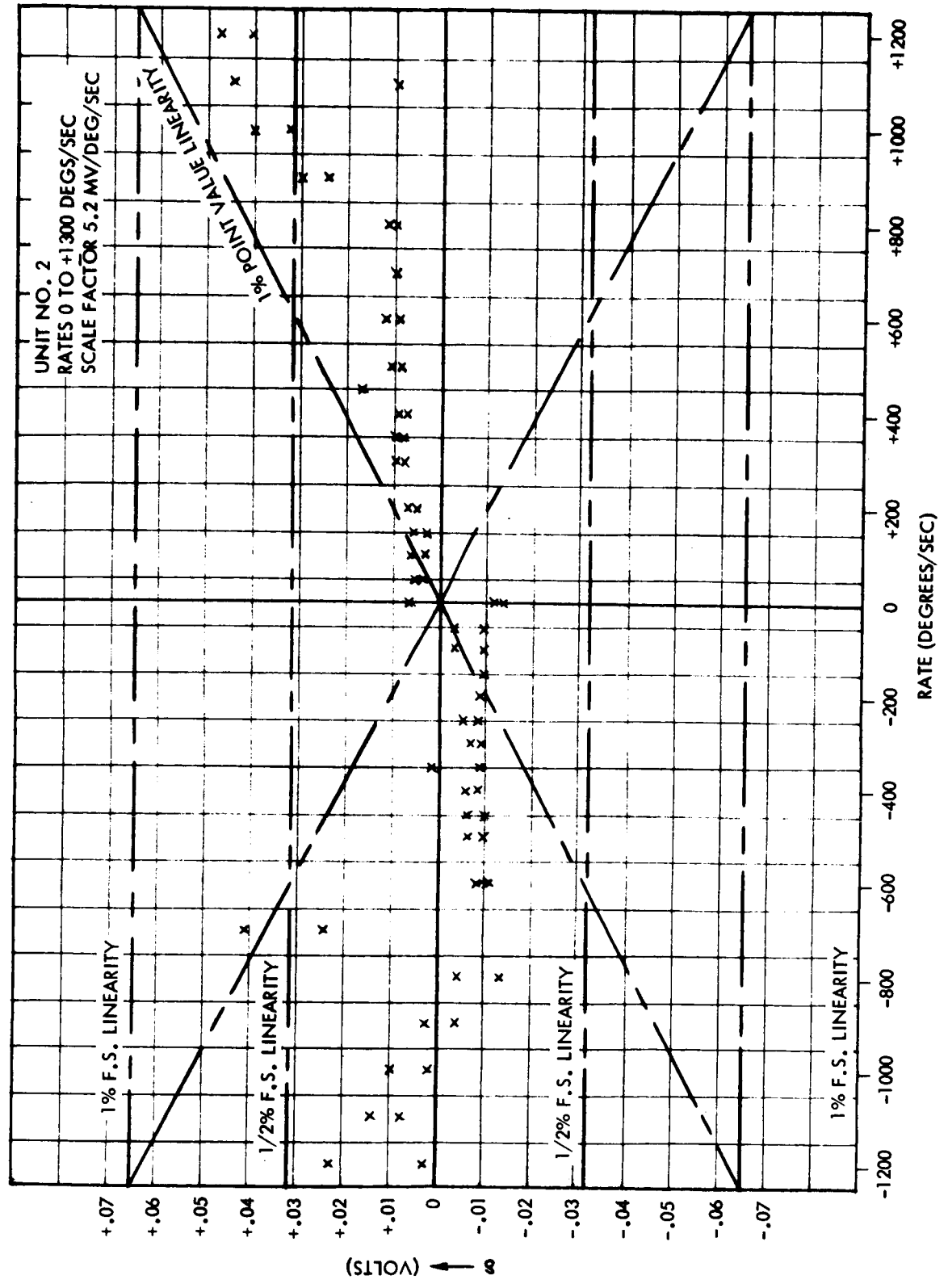

Figure 23. Linearity Deviations (Unit No. 2) 0 to ±1200 Degs/Sec.

Thus, for a 200 deg/sec change in cross axis rate, the total output voltage change was .0088 volts. For a rate input of 200 deg/sec about the sensitive axis the output voltage would have been 14.4 volts. Thus, the rate cross coupling was equal to:

$$\frac{.0088}{14.4} = .00061 = .06\%$$

With a more careful adjustment of the shims or other precise alignment of the gyro, the cross coupling could certainly be reduced below this value. Similar results were obtained with unit No. 2.

LONG TERM DRIFT TESTS

Extensive long term testing of the solid state rate sensors has been performed with the results tabulated in Table 3. These tests were of time durations varying from forty-eight hours to one hundred fourteen hours. No tests were terminated due to failures of any sort, nor did any failures occur during these or other long term tests. The results were recorded using a Rustrak recorder driven by a Kintel microvoltmeter which was connected to the output of the rate sensor demodulator. The type of null stability existing with the rate sensor is shown by the typical Rustrak recording shown in Figure 24. This trace shows the actual recorded sensor null between hours 56 and 62 of run A shown in Table 3.

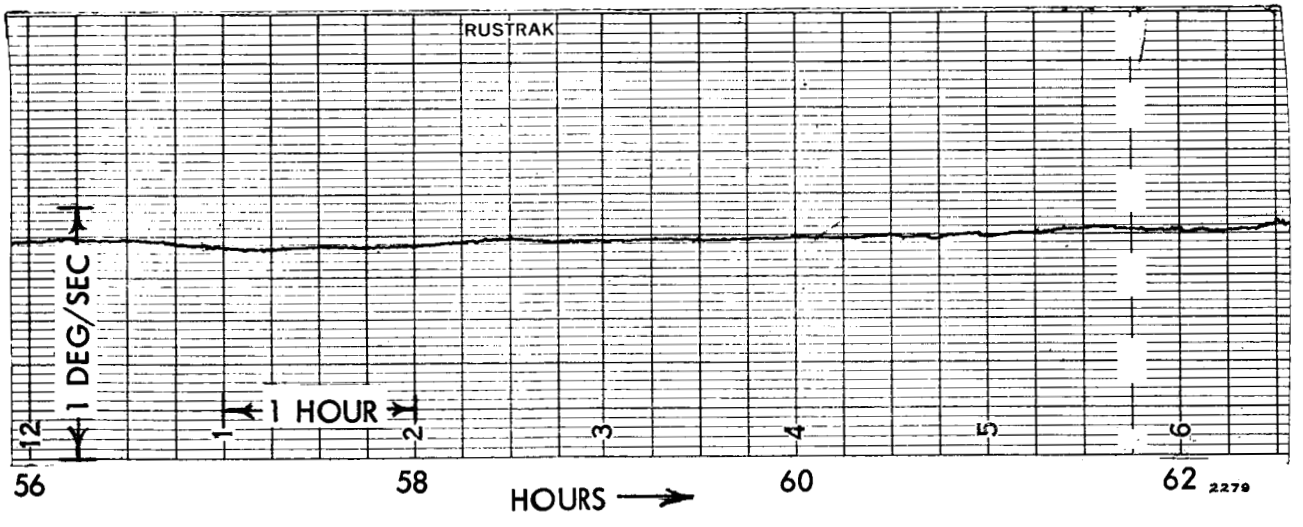

Figure 24. Recording of Long Term Null (Unit No. 1)

TABLE 3

LONG TERM DRIFT TESTS

Time (Hours)	CUMULATIVE DRIFT IN DEGREES/SEC				
	Run A	Run B*	Run C*	Run D	Run E
0	0 (deg/sec)	0 (deg/sec	0 (deg/sec)	0 (deg/sec)	0 (deg/sec)
	.27	+.26	+1.14	.20	.08
4	.39	+.28	+ .82	.23	.13
	.28	+.22	+ .61	.27	.18
8	.28	+.14	+ .40	.31	.20
	.28	+.03	+ .30	.33	.23
12	.28	-.03	+ .18	.36	.28
	.28	-.08	+ .31	.38	.33
16	.28	+.01	+ .18	.40	.38
	.24	-.07	+ .23	.43	.41
20	.23	-.01	+ .23	.45	.43
	.25	+.06	+ .12	.46	.48
24	.27	+.08	+ .26	.48	.53
	.30	+.03	- .05	.50	.56
28	.32	-.01	+ .05	.51	.58
	.36	0	+ .05	.54	.61
32	.40	+.06	- .09	.54	.63
	.42	-.08	- .05	.55	.66
36	.40	-.04	+ .05	.57	.69
	.42	-.17	- .03	.58	.71
40	.42	-.08	- .30	.59	.72
	.39	-.14	- .23	.60	.76
44	.40	-.16	- .30	.62	.79
	.46	-.16	- .23	.64	.80
48	.49	-.15	- .14	.66	.81
	.53	-.16	- .18		.84
52	.56	-.15	- .40		.86
	.60	-.21	- .18		.89
56	.65	-.17	- .40		.91
	.63	-.15	- .30		.94
60	.66	-.13	- .47		.96
	.68	-.14	- .53		.99
64	.70		- .30		.90
			- .23		1.02
68			- .30		1.00
			- .30		.97
72			- .40		1.12
			- .40		1.19
76			- .58		1.19
			- .32		1.23
80			- .39		1.27
			- .47		1.27
84			- .53		1.32
86			- .67		1.35
94					1.40
104					1.50
114					1.56

*Polarity indicated only to show that a reversal occurred during the run. The choice of plus and minus is arbitrary.

The numbers in Table 3 show the recorded null voltage values converted to equivalent degrees/sec of null shift.

Runs A and B are long term drift tests on unit No. 1. This unit, as noted before, utilized low impedance buffer amplifiers. Run A was one of the earliest tests on this unit. After all other tests including the temperature and "G" loading test were made, Run B was made. It is interesting to compare these runs and note that Run A shows a general tendency to increase in one direction, whereas, Run B is more random in nature, drifting first plus then minus etc.

Run C was obtained from a hybrid unit using No. 1 beam and No. 2 electronics. This used the high impedance readout buffers with the No. 1 beam. This run provides an interesting comparison with Run B which used the same beam but the low impedance buffer amplifiers. The two tests were run sequentially. Run B was random in nature with null uncertainties of approximately ±.3 deg/sec. Run C peaks at +1.14 deg/sec null shift at the end of two hours and then drifts relatively uniformly at a rate of -.02 deg/sec/hr. This uniform drift seemed to be consistently obtained with the high impedance buffer amplifiers, whereas the random drift was more characteristic of the low impedance electronics. Run D is a test of unit No. 2 (high impedance) which again shows the drift buildup. Ignoring the first two hours of stabilization, the average drift is .01 deg/sec/hr, or including the first two hours, the average drift is .014 deg/sec/hr for the forty-eight hour run.

Run E is a 114 hour drift run utilizing an early development beam fabricated on the present contract and high-impedance breadboard electronics. This run again shows the drift buildup with an average gradient of .014 deg/sec/hr.

OPERATIONAL LIFE

While no formal life testing of the solid state gyros has been done, indications are that operational periods in excess of one year should be realistic.

Both breadboard units have been run on an on-off test basis over a period of two months including several tests in excess of 60 hours. There have been no operational failures. In general, the units were left on at night after the days testing was completed. Again, no failures occurred. An earlier version gyro built near the beginning of this contract has operated, and is still operating satisfactorily. It has run for considerable periods of time, including a 114 hour drift run over a five day period, and no change in its performance is discernible. Two other units which were

built prior to the present contract and are used in suitcase demonstrators have been operational for well over a year. They have been flown, carried and shipped to many parts of the United States without an operational failure.

ENVIRONMENTAL TESTS

TEMPERATURE

Extensive temperature testing of the two solid state rate gyros has been performed and significant improvements have been made in performance as compared to that at the beginning of this contract. However, the present results are far from satisfactory and a varying temperature environment remains a major problem area. At the start of this contract a temperature test would generally result in sensor null shifts which would saturate the electronics (200°/sec +). At the present time, similar tests are over an order of magnitude better with results of ±5 deg/sec generally obtainable.

The major problem is that the results show poor repeatability from one run to the next and the degree of nonrepeatability is quite large.

Table 4 below presents five consecutive temperature cycles on unit No. 1 where the temperature was changed from 30°C to 55°C allowed to stabilize then changed to 75°C, again allowed to stabilize and then the oven was shut off and the unit left to return to room temperature. The null voltages were recorded on a Rustrak recorder and were allowed to stabilize prior to the taking of the null reading. The time interval between readings at a given temperature was maintained constant in order to achieve the best possible repeatability. The average time between readings was approximately 30 minutes. The values given in the table are the null shift voltages converted to equivalent degrees/sec.

TABLE 4

TEMPERATURE CYCLE NO.

(Temperature °C)	1	2	3	4	5	6*	
30°	0.0 deg/sec	+ .7	+.4	+ .7	+ .2	+ .8	30°C
						+2.43	40°C
						+1.84	50°C
55°	-1.4	- .1	-.7	+1.0	+ .7		
						- .94	60°C
						-7.23	70°C
75°	-5.6	-7.4	omitted	-7.9	-7.6		
30°	+ .7	+ .4	+.7	+ .2	+ .8		

*Run No. 6 was run immediately after No. 5; however, different temperature intervals were used as indicated.

The results shown in this table are representative of those generally obtained. However, both significantly worse and significantly better results have been obtained on occasion on this same unit and on others.

Table 5 below shows another temperature test run on unit No. 1. Here the temperature was increased approximately 5°C every 10 minutes. The temperature was measured with a thermocouple mounted directly on the beam mount. As will be noted, the increasing part of the cycle showed less than 1 deg/sec of null shift between 25°C and 72°C.

TABLE 5

TEMPERATURE TEST (UNIT NO. 1)

Time (Mins)	Temperature (°C)	Null Variations (Equiv. Degs/Sec)
0	25	0
10	29	- .20
20	40	+ .10
30	45	- .18
40	50	- .62
50	55	- .56
60	60	- .65
70	67.5	- .35
80	72	- .54
90	60	+1.60
100	52	+5.09
110	46	+1.71
120	41	- .18
130	36	- .85

However, as soon as the temperature was decreased, significant null shifts occurred.

It is believed that further effort directed toward the temperature problem will result in significant improvements in temperature performance. The solid state rate sensor is extremely sensitive to thermal gradients, but to date, little effort has been directed toward packaging the unit to eliminate these gradients. Further improvements should arise by operating the sensor in a partial vacuum, by improving the mount and lead dress, and by testing and selectively choosing the piezoelectric crystals used on the beam.

It should be noted that the beam assembly is mounted to the sensor package in a manner to eliminate any stressing of the beam mount due to thermal effects.

SCALE FACTOR CHANGE WITH TEMPERATURE

Several tests were run to determine the variation of scale factor over the temperature range 25°C to 70°C. Results indicate that this varies between 5 and 10 percent over this range, depending on the particular unit. At the start of the contract the variation was on the order of 100 percent. The improvement has resulted from the incorporation of a regulator circuit to maintain constant feedback voltage and an improved bond between the crystal and the beam.

"G" SENSITIVITY

The present test program has pointed out that a sensitivity to "G loading" exists with the present solid state rate-of-turn sensors.

While, theoretically, the free-free beam is insensitive to "G loading", the practical difficulty in building a true free-free beam results in a "G" sensitive device. It is believed that significant improvements can be made in this area by a redesign of the beam mount. This would be located nearer to the neutral fiber of the beam and would be precisely positioned at the true nodes of the vibrating system.

The principle "G" sensitivity tests were run on a Genesco rate table with the rate sensor mounted twelve inches from the axis of rotation. The longitudinal axis of the gyro was mounted tangent to the circumference of the table. This allowed "G" loadings of up to 10G to be obtained.

The solid curve in Figure 25 shows the measured sensor output of unit No. 1 as a function of angular rate input. This curve has a small linear component, a "G" component and a "G^2" component as its predominant parts. The linear component is due to a slight misalignment of the sensor on the table which allowed some coupling of the rate table notion into the sensitive axis of the sensor. On the assumption that this curve would be made up primarily of the three components just discussed, (linear, "G" and "G^2"), and knowing that No. g's $= \frac{R\omega_g^2}{32.2}$ an equation of the form

$$E = \overbrace{a\,\omega_g}^{\text{linear}} + \overbrace{b\omega_g^2}^{\propto G} = \overbrace{c\,\omega_g^4}^{\propto G^2}$$

can be fitted to this data. The equation given below provides a satisfactory fit to ±800 deg/sec.

$$E = 5.44\,\omega_g - .718\,\omega_g^2 + .00439\,\omega_g^4$$

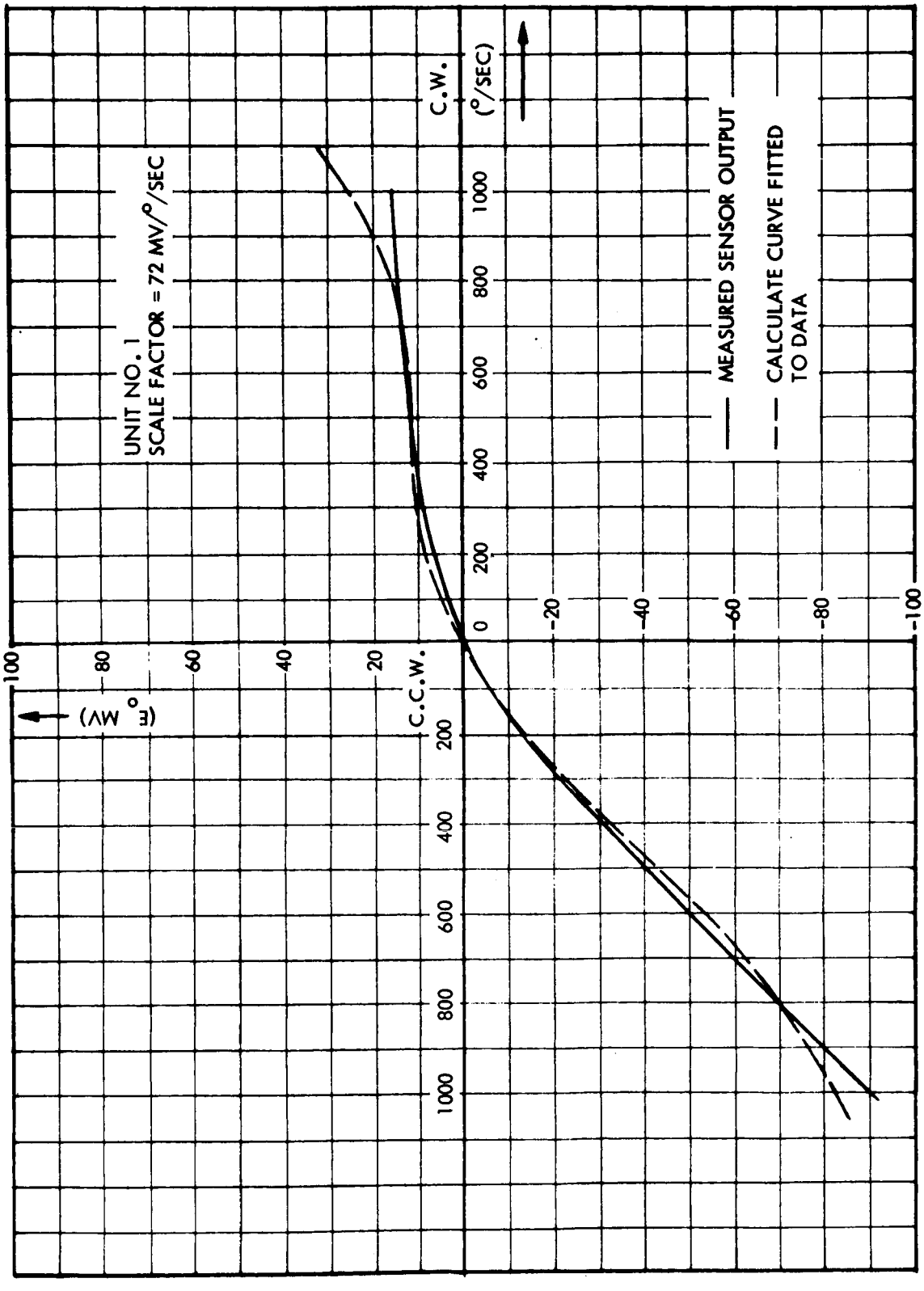

Figure 25. G Loading Tests (Unit No. 1)

where E is in millivolts
ω_g is in units of (100 deg/sec)

This equation has been evaluated and is shown by the dotted line in Figure 25.

Omitting the linear term which is due to rate coupling leaves an expression for the "G" sensitivity of unit No. 1 (very similar results were obtained with unit No. 2).

$$E_G = -.718\ \omega_g^2 + .00439\ \omega_g^4$$

The ω^2 term is proportional to "G" and the ω^4 term is proportional to "G^2". Each of these terms is plotted independently in Figure 26 and their sum representing the resultant output due to "G" loading is also shown there.

Converting the ω scale to G and replotting the two components of the derived equation yield the results shown in Figure 27. Here, it can be seen that the sensor output due to "G" is approximately 7.7 mv/G. At the time of this test the scale factor of the unit was 72 mv/deg/sec. Hence, the "G" sensitivity of this unit for loading perpendicular to the longitudinal axis of the beam is .1/deg/sec/G. The G^2 sensitivity can be found similarly and for this unit is .06 deg/sec/G^2.

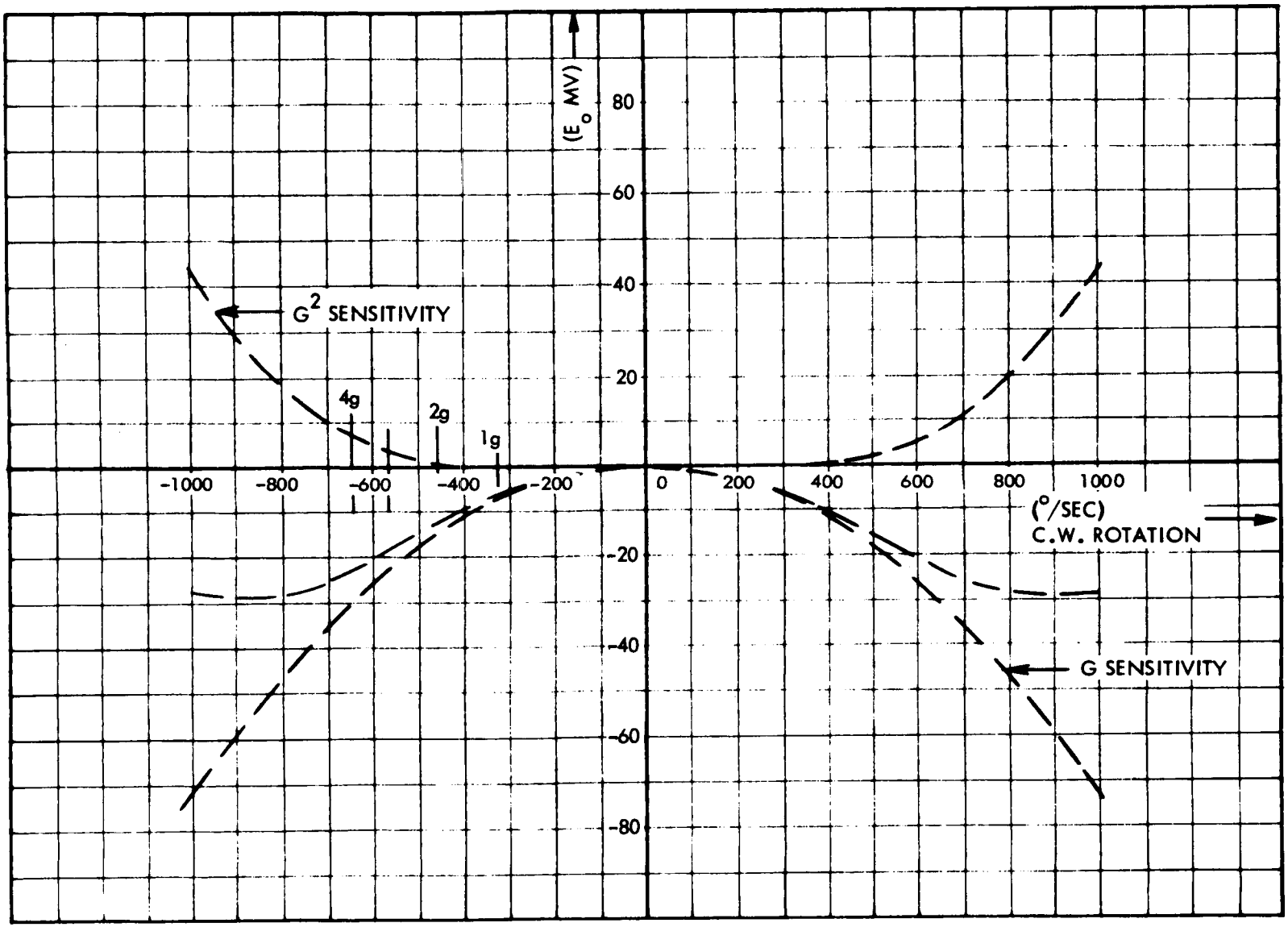

Figure 26. Calculated G and G^2 Sensitivity Terms as a Function of ω

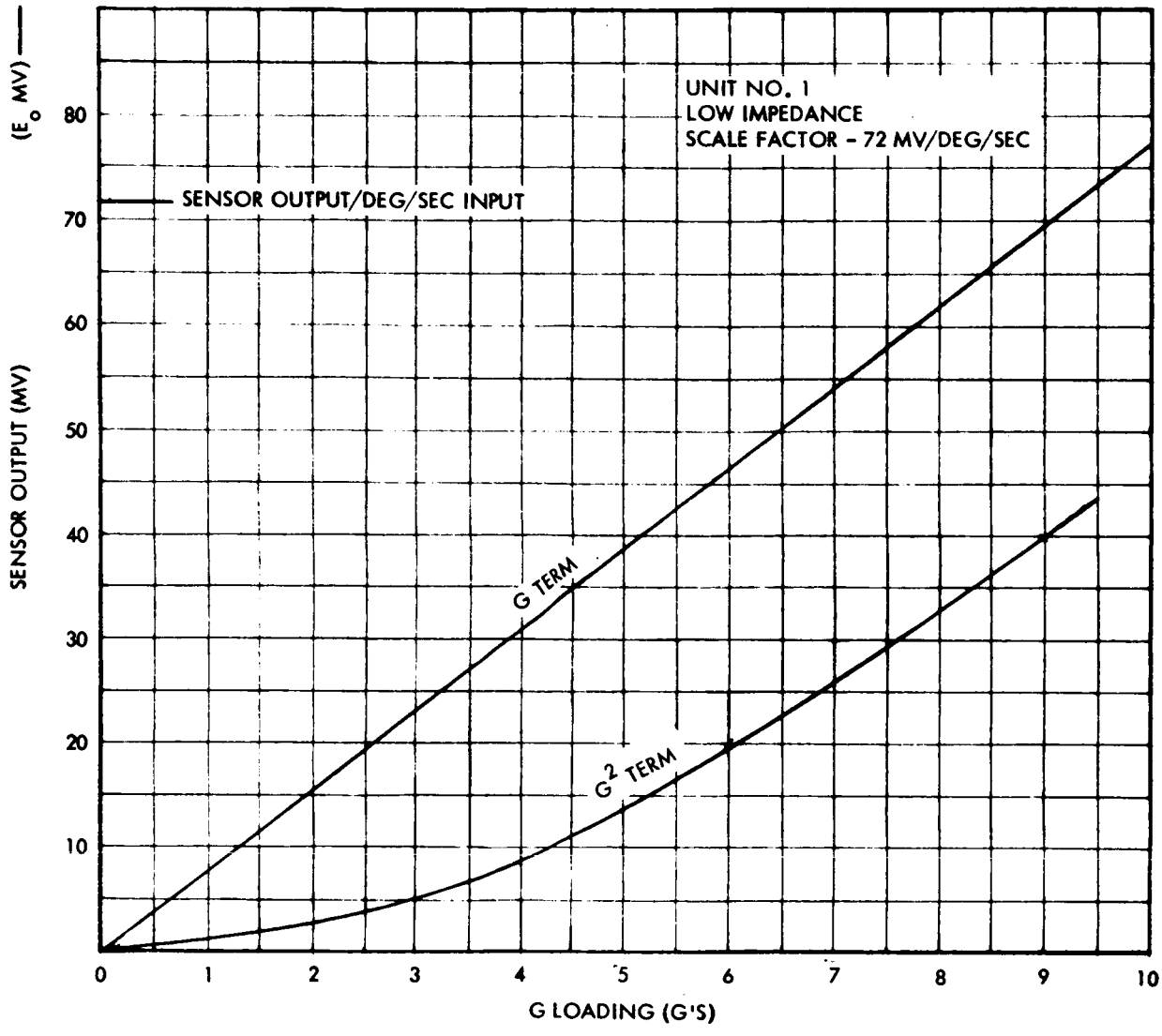

Figure 27. Calculated G and G^2 Sensitivity Terms as a Function of G

Section 8

CONCLUSIONS

The results of this contract effort have demonstrated that a vibrating beam rate gyro can be built with predictable operating characteristics with an accuracy comparable to that of a large range of flight control rate gyros under laboratory type environments. The simplicity and reliability of the basic sensor element and the low power requirements coupled with superior bandwidth of the solid state gyro compare very favorably with conventional rate gyros. The wide dynamic range and good linearity of the solid state gyro provide additional plus factors.

Environmental tests, however, have shown that temperature drift must be improved to provide comparable performance to existing rate gyros. This would be one of the main areas for investigation for a following phase of this program. The inherent high Q operation of the sensor results in high shock sensitivity at the beam separation frequency. Providing the required damping will constitute the second major effort during the next phase of the program.

The current development work has demonstrated operation primarily in a laboratory environment to which its predictable use is now restricted.

Further development effort will improve threshold values, temperature effects, and g tolerance to a point where it can be used in applications where conventional rate sensors apply, principally control systems, instrumentation and displays. Special application areas such as reentry instrumentation and control, small satellite use and long duration missions can benefit by solid state rate sensor features of low power, long life, wide dynamic range, and improved bandwidth.

μA709C

HIGH PERFORMANCE OPERATIONAL AMPLIFIER

FAIRCHILD LINEAR INTEGRATED CIRCUITS

GENERAL DESCRIPTION - The μA709C is a High-Gain Operational amplifier constructed on a single silicon chip using the Fairchild Planar epitaxial process. It features low offset, high input impedance, large input common mode range, high output swing under load and low power consumption. The device displays exceptional temperature stability and will operate over a wide range of supply voltages with little degradation of performance. The amplifier is intended for use in DC servo systems, high impedance analog computers, in low-level instrumentation applications and for the generation of special linear and nonlinear transfer functions. For full temperature range (-55°C to +125°C) see μA709 data sheet.

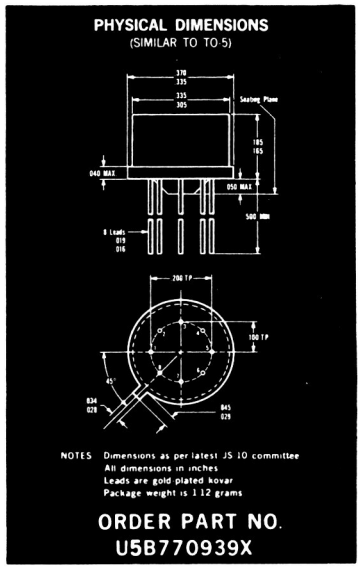

ABSOLUTE MAXIMUM RATINGS

Supply Voltage		± 18 Volts
Internal Power Dissipation	(Note 1)	250 mW
Differential Input Voltage		± 5.0 Volts
Input Voltage		± 10 Volts
Output Short-Circuit Duration	(T_A = 25°C)	5 sec
Storage Temperature Range		-65°C to +150°C
Operating Ambient Temperature Range		0°C to +70°C
Lead Temperature (Soldering, 60 sec)		300°C

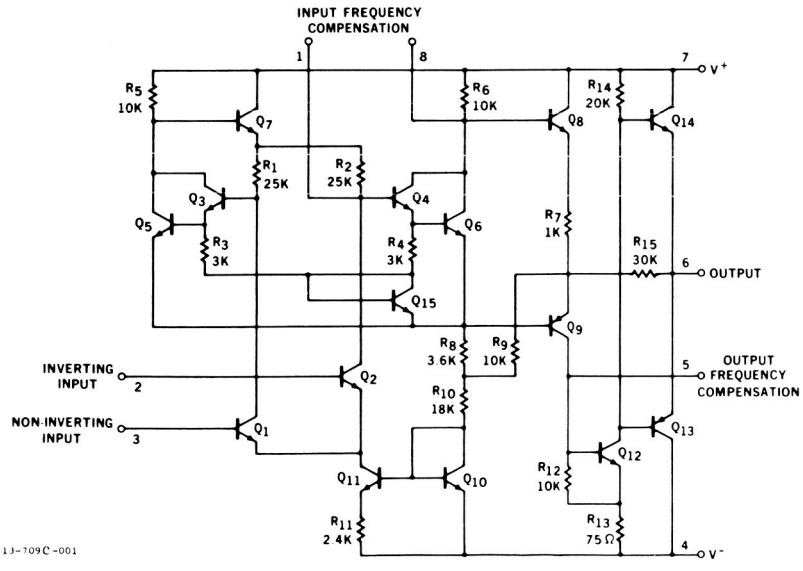

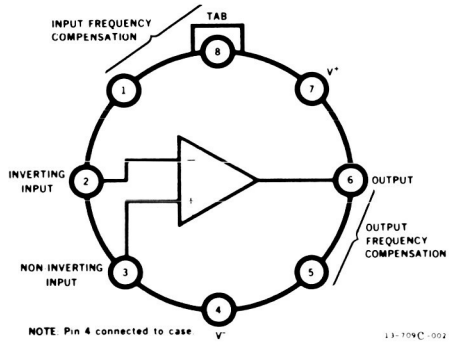

CONNECTION DIAGRAM
(TOP VIEW)

NOTE 1: Rating applies for case temperatures to +70°C; derate linearly at 5.6 mW/°C for ambient temperatures above +55°C.

313 FAIRCHILD DRIVE, MOUNTAIN VIEW, CALIFORNIA, (415) 962-5011, TWX: 910-379-6435

FAIRCHILD SEMICONDUCTOR
A DIVISION OF FAIRCHILD CAMERA AND INSTRUMENT CORPORATION

ELECTRICAL CHARACTERISTICS (V_S = ±15 V, T_A = 25°C Unless Otherwise Specified)

Parameter	Conditions	Min.	Typ.	Max.	Units
Input Offset Voltage	$R_S \leq 10\,K$, $\pm 9\,V \leq V_S \leq \pm 15\,V$		2.0	7.5	mV
Input Offset Current			100	500	nA
Input Bias Current			0.3	1.5	μA
Input Resistance		50	250		KΩ
Output Resistance			150		Ω
Large-Signal Voltage Gain	$R_L \geq 2\,K$, $V_{OUT} = \pm 10\,V$	15,000	45,000		
Output Voltage Swing	$R_L \geq 10\,K$	±12	±14		V
	$R_L \geq 2\,K$	±10	±13		V
Input Voltage Range		±8.0	±10		V
Common Mode Rejection Ratio	$R_S \leq 10\,K$	65	90		db
Supply Voltage Rejection Ratio	$R_S \leq 10\,K$		25	200	μV/V
Power Consumption			80	200	mW
The following specifications apply for $0°C \leq T_A \leq +70°C$					
Input Offset Voltage	$R_S \leq 10\,K$, $\pm 9\,V \leq V_S \leq \pm 15\,V$			10	mV
Input Offset Current				750	nA
Input Bias Current				2.0	μA
Large-Signal Voltage Gain	$R_L \geq 2\,K$, $V_{OUT} = \pm 10\,V$	12,000			

GUARANTEED ELECTRICAL CHARACTERISTICS

VOLTAGE GAIN

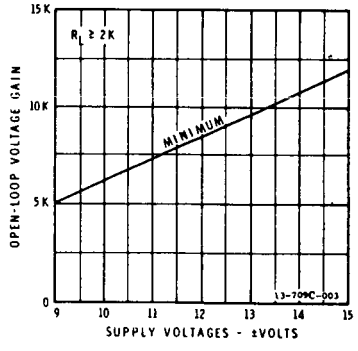

OUTPUT SWING

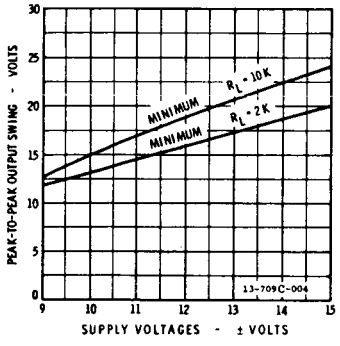

INPUT COMMON MODE VOLTAGE RANGE

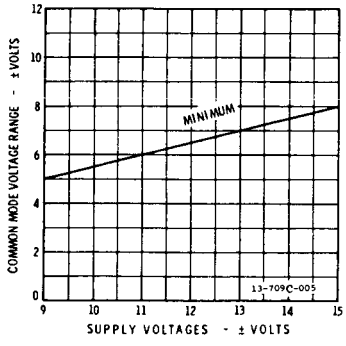

TYPICAL PERFORMANCE CURVES

VOLTAGE TRANSFER CHARACTERISTIC

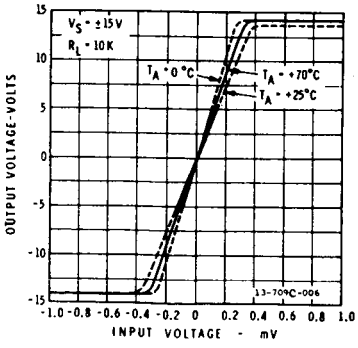

FREQUENCY COMPENSATION CIRCUIT

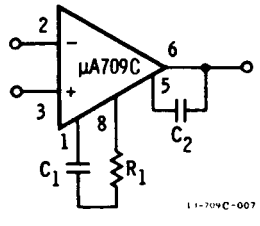

FREQUENCY RESPONSE FOR VARIOUS CLOSED-LOOP GAINS

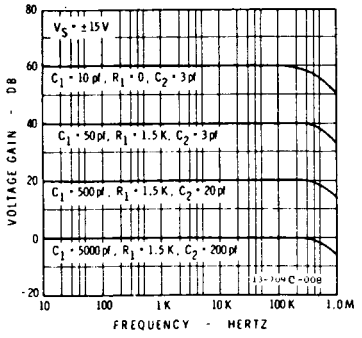

Appendix B

FREE LATERAL VIBRATION OF A FREE-FREE BEAM

The partial differential equation for the deflection x(z, t) of a vibrating beam of uniform cross-section such as shown in Figure B-1 is

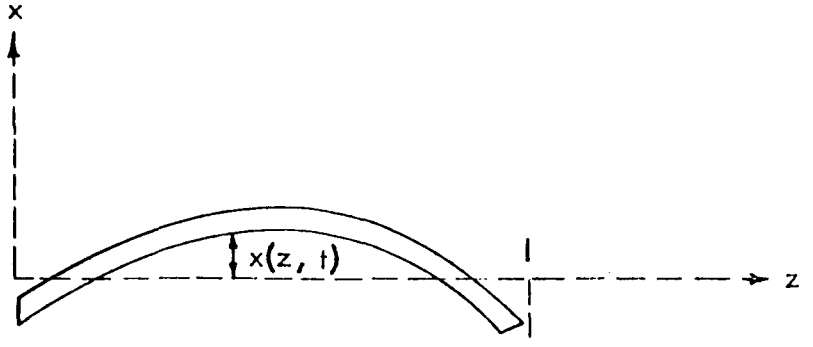

Figure B-1. Free-Free Beam

$$EI \frac{\partial^4 x(z,t)}{\partial z^4} = -\mu \frac{\partial^2 x(z,t)}{\partial t^2}$$ (page 324 of reference 1)

where μ is the mass of the beam per unit length and EI is flexural rigidity. The solution of the above equation is found by assuming a solution of the form

$$x(z,t) = H(z) \sin \omega t$$

Therefore

$$EI \frac{d^4 H(z)}{dz^4} \sin \omega t = +\omega^2 \mu H(z) \sin \omega t$$

or

$$\frac{d^2H(z)}{dz^4} - \frac{\omega^2\mu}{EI} H(z) = 0$$

Define $$k^4 = \frac{\omega^2\mu}{EI}$$

then $$\frac{d^4H(z)}{dz^4} - k^4 H(z) = 0$$

The general solution of the preceeding equation is found by Laplace transform techniques and is

$$H(z) = A_1 \cos kz + A_2 \sin kz + A_3 \cosh kz + A_4 \sinh kz$$

where the A's are arbitrary constants.

The solution of this problem for the particular case of the free-free beam is found by applying the boundary conditions

$$(1) \quad \left[\frac{d^2H(z)}{dz^2}\right]_{z=0} = 0$$

$$(2) \quad \left[\frac{d^3H(z)}{dz^3}\right]_{z=0} = 0$$

$$(3) \quad \left[\frac{d^2H(z)}{dz^2}\right]_{z=\ell} = 0$$

$$(4) \quad \left[\frac{d^3H(z)}{dz^3}\right]_{z=\ell} = 0$$

The conditions above state that the shape of the beam at any time t must be such that the bending moment and shearing force vanish at the ends. By applying conditions (1) and (2), we find that

$$A_1 = A_3 \text{ and } A_2 = A_4$$

so that

$$H(z) = A_1 (\cos kz + \cosh kz) + A_2 (\sin kz + \sinh kz)$$

Applying conditions (3) and (4), we obtain the two equations

$$A_1 (\cosh k\ell - \cos k\ell) + A_2 (\sinh k\ell - \sin k\ell) = 0$$

$$A_1 (\sinh k\ell + \sin k\ell) + A_2 (\cosh k\ell - \cos k\ell) = 0$$

A non-trivial solution of these equations for the constants A_1 and A_2 requires that the determinant of the coefficient matrix be equal to zero.

$$(\cosh k\ell - \cos k\ell)^2 - (\sin h^2 k\ell - \sin^2 k\ell) = 0$$

or $$\cos k\ell \cosh k\ell = 1$$

The roots of this equation are the eigenvalues of the problem which determine the resonant frequencies of the beam. The first six roots of the equation are

$$k\ell = 0,\ 4.730,\ 7.853,\ 10.996,\ 14.137,\ 17.279$$

For $$k\ell = 0,\ k = 0 \text{ and } \omega = k^2 \left(\frac{EI}{\mu} \right)^{1/2} = 0$$

$$H(z) = 2A_1 = \text{constant}$$

$$x(z, t) = H(z) \sin \omega t = 0$$

For $$k\ell = 4.73,\ K = \frac{4.73}{\ell},\quad \omega = \frac{22.4}{\ell^2} \left(\frac{EI}{\mu} \right)^{1/2}$$

$$\frac{A_2}{A_1} = \frac{\cosh 4.73 - \cos 4.73}{\sin 4.73 - \sinh 4.73} \cong -1$$

$$H(z) = A_1 \left(\cos \frac{4.73z}{\ell} + \cosh \frac{4.73z}{\ell} - \sin \frac{4.73z}{\ell} - \sinh \frac{4.73z}{\ell}\right)$$

The above shape of the beam for the first bending mode as given by H(z) is the normal elastic curve for a free-free beam. Note that the curve has a translation and rotation with respect to the z-axis due to constant and first degree terms in z which are also solutions of the partial differential equation.

An approximation to the elastic curve with the rotational terms removed is

$$H(z) = x_o \sin \frac{\pi z}{\ell} - a^* \quad \text{(Rayleigh's approximation for the free-free beam first mode shape)}$$

The approximate solution for x(z, t) for the first mode is

$$x(z,t) = H(z) \sin \omega t$$

$$x(z,t) = \left(x_o \sin \frac{\pi z}{\ell} - a\right) \sin \omega t$$

where $$\omega = \frac{22.4}{\ell^2} \left(\frac{EI}{\mu}\right)^{1/2}$$

and a is a constant that determines the location of the nodes.

The actual value of 'a' can be found from the fact that since no external alternating force is acting on the beam, its total vertical momentum must be zero. When the beam passes through its equilibrium position, the ends have downward velocities and the middle has an upward velocity. The total momentum is zero for all t if the areas above and below the z-axis are equal.

For $$\omega t = \frac{\pi}{2}$$

$$0 = \int_0^{\ell} x(z)dz = x_o \int_0^{\ell} \sin \frac{\pi z}{\ell} \, dz - \int_0^{\ell} a \, dz$$

*Derivation and use of Rayleigh's method is given in Reference 2, pages 141 - 146 and 161 - 162.

Therefore,

$$a = \frac{2x_o}{\pi}$$

and

$$x(z,t) = x_o \left[\sin \frac{\pi z}{\ell} - \frac{2}{\pi} \right] \sin \omega t$$

The nodes are located at the points where

$$\sin \frac{\pi z}{\ell} - \frac{2}{\pi}$$

or $z = 0.22\ell$

$z = 0.78\ell$

REFERENCES

1. Timoshenko, S., "Vibration Problems in Engineering," 3rd Edition.

2. DenHartog, J. P., "Mechanical Vibrations," 4th Edition 1956.